








# Holographic Imaging With XL-MIMO and RIS: Illumination and Reflection Design

G. Torcolacci , Graduate Student Member, IEEE, A. Guerra , Member, IEEE, H. Zhang , Member, IEEE, F. Guidi , Member, IEEE, Q. Yang , Graduate Student Member, IEEE, Y. C. Eldar , Fellow, IEEE, and D. Dardari , Senior Member, IEEE

**Abstract**—This paper addresses a near-field imaging problem utilizing extremely large-scale multiple-input multiple-output (XL-MIMO) antennas and reconfigurable intelligent surfaces (RISs) already in place for wireless communications. To this end, we consider a system with a fixed transmitting antenna array illuminating a region of interest (ROI) and a fixed receiving antenna array inferring the ROI's scattering coefficients. Leveraging XL-MIMO and high frequencies, the ROI is situated in the radiative near-field region of both antenna arrays, thus enhancing the degrees of freedom (DoF) (i.e., the channel matrix rank) of the illuminating and sensing channels available for imaging, here referred to as *holographic imaging*. To further boost the imaging performance, we optimize the illuminating waveform by solving a min-max optimization problem having the upper bound of the mean squared error (MSE) of the image estimate as the objective function. Additionally, we address the challenge of non-line-of-sight (NLOS) scenarios by considering the presence of a RIS and deriving its optimal reflection coefficients. Numerical results investigate the interplay between illumination optimization, geometric configuration (monostatic and bistatic), the DoF of the illuminating and sensing channels, image estimation accuracy, and image complexity.

**Index Terms**—Holographic imaging, XL-MIMO, illumination design, near-field, reconfigurable intelligent surfaces.

## I. INTRODUCTION

THE rapid progress of wireless communication systems has laid the foundation for the forthcoming generation of

Manuscript received 14 December 2023; revised 13 May 2024; accepted 3 June 2024. Date of publication 20 June 2024; date of current version 1 November 2024. The work of Giulia Torcolacci was supported by NRRP Ph.D. grant. This work was supported in part by the European Union under the Italian National Recovery and Resilience Plan (NRRP) of NextGenerationEU, partnership on Telecommunications of the Future (PE00000001 - program RESTART), in part by the EU Horizon project TIMES under Grant 101096307, in part by the Nanjing Overseas Students Science and Technology Innovation Project under Grant NJKCZYZZ2023-01, and in part by ERC-STG-2023 project CUE-GO under Grant 101116257. The guest editor coordinating the review of this manuscript and approving it for publication was Dr. Ahmet M. Elbir. (Corresponding author: G. Torcolacci.)

G. Torcolacci and D. Dardari are with the Department of Electrical, Electronic, and Information Engineering “Guglielmo Marconi” - DEI-CNIT, University of Bologna, 47521 Cesena FC, Italy (e-mail: g.torcolacci@unibo.it; davide.dardari@unibo.it).

A. Guerra and F. Guidi are with the National Research Council of Italy, Institute of Electronics, Computer and Telecommunication Engineering, 40126 Bologna, Italy (e-mail: anna.guerra@cnr.it; francesco.guidi@cnr.it).

H. Zhang and Q. Yang are with the School of Communication and Information Engineering, Nanjing University of Posts and Telecommunications, Nanjing 210023, China (e-mail: haiyang.zhang@njupt.edu.cn; 2020010207@njupt.edu.cn).

Y. C. Eldar is with the Faculty of Math and CS, Weizmann Institute of Science, Rehovot 234, Israel (e-mail: yonina.eldar@weizmann.ac.il).

Digital Object Identifier 10.1109/JSTSP.2024.3417356

networks, referred to as 6th Generation (6G) systems, which will integrate and synergize localization, sensing, and communications. This convergence is commonly referred to as integrated sensing and communications (ISAC) [1], [2]. These capabilities are enabled by high-frequency bands and electrically large antenna arrays, e.g., based on metasurfaces and XL-MIMO antennas [3], [4], [5], [6]. As a result, 6G systems are expected to mainly operate in the radiative near-field region, enabling unprecedented levels of communication and sensing performance, flexibility, and resolution [7], [8], [9]. In this context, significant research contributions have shed light on the potential of holographic communications [10], [11], [12], [13], localization [14], [15], [16], [17], sensing [18], [19], and imaging [20].

While the benefits of operating in the near-field propagation regime have been extensively demonstrated for localization, communication, and sensing, the potential advantages of performing holographic imaging within wireless communication networks have been largely unexplored to date. This work aims to investigate the capabilities of near-field imaging, shedding light on its potential in 6G scenarios where RISs are also employed to cope with NLOS channel conditions [21], [22].

With *holographic imaging*, we hereby refer to the possibility of estimating the reflective properties of a ROI using XL-MIMO systems operating in the near-field. The procedure involves initially illuminating the ROI, represented as a pixel-based image, and then capturing its backscattered electromagnetic (EM) field through the receiving array. Thanks to the near-field propagation regime, which allows for the extraction of both depth and angular information compared to the far-field and hence increasing the number of exploitable DoF [23], more informative measurements can be collected from the ROI, thus leading to improved imaging capabilities.

Conventional radio imaging techniques, typically employed for medicine, biology, geology, and engineering, use EM fields to create 3D images of physical entities using dedicated infrastructures. The common approach is to address an inverse scattering problem (ISP), where the primary objective is to extract features related to potential scatterers in a given ROI by analyzing the scattered EM field [24], [25]. The primary challenge in such problems lies in their ill-posed nature, necessitating the incorporation of regularization techniques for their effective resolution [26]. Various technologies and transmission techniques have been systematically explored to minimize reconstruction errors and enhance target images' resolution. Examples include

synthetic aperture radar (SAR) [27], [28], [29], [30], classic holography [31], [32], MIMO antennas [33], [34], [35], computational imaging [36], [37], [38], and others [39], [40], [41]. Notably, many specialized algorithms have been devised for image retrieval, each exhibiting advantages and disadvantages. For instance, a range of methodologies exist in the domain of SAR-based methods, including back-propagation [42], [43], range migration [27], [44], range-Doppler [28], chirp-scaling [45], as well as inverse/stripmap/tomographic/spotlight SAR algorithms [46], [47], [48]. Furthermore, a multitude of widely adopted strategies and approximations, such as Stolt interpolation [49], stationary phase method [50], and many others, assume pivotal roles in enhancing imaging precision and dependability across diverse applications. Deep learning techniques have also recently been applied to near-field imaging in [51], [52], [53].

Regarding the operational frequencies and devices, imaging is frequently performed using microwaves or visible light technologies, like lidars [54], [55]. In this regard, only a few works have explored the use of systems primarily designed for wireless communications to perform imaging of unknown objects [30], [40], [56], [57], [58] [59], [60].

Indeed, most imaging approaches proposed in the literature require illuminating and sensing the backscattered EM field from a large set of angles through the deployment of a dedicated imaging infrastructure typically working in the far-field region. Hence, their applicability in next-generation wireless systems endowed with ISAC capabilities is limited.

When addressing NLOS imaging, methods have been devised to effectively illuminate stationary objects, such as walls, to enable target reconstruction [61]. In light of the foreseen 6G scenarios, we explore the possibility of using RISs for holographic imaging in line-of-sight (LOS) conditions by optimizing their reflective characteristics to control the propagation channel [62] and backscatter the illumination towards the ROI. In [62], the authors present an approach for computational imaging using a RIS, based on distributed antenna systems and stochastic modulation of detecting signals. Their work predominantly operates within the far-field regime, thus neglecting the large number DoF available in the near-field region facilitated by the spherical EM wavefront propagation. In [63], the authors present a method for near-field computational imaging that integrates a RIS with holographic aperture technology, where the RIS is used to generate multiple virtual EM masks on the target ROI. This RIS operates as an active reflector, amplifying and reflecting the impinging signals, thus requiring a higher complexity and elevated hardware costs.

To the authors' best knowledge, investigation of illumination and RIS optimization strategies when operating in the near-field region has not yet been tackled in the literature. To fill this gap, in our paper, we consider near-field imaging (*holographic imaging*) leveraging XL-MIMO, RIS, and high-frequency bands within the context of next-generation wireless systems. In particular, we propose an analytical framework that captures the distinctive features of the available DoF of the near-field channel and the presence of a RIS to enhance imaging performance in NLOS scenarios. Our main contributions are as follows.

- *Illumination Waveform Design:* We enhance holographic imaging by optimizing the transmitting waveform for improved ROI illumination, particularly with signals tailored for wireless communications and near-field propagation. We propose an optimization approach that searches for the illumination signal minimizing the MSE of the image estimate. To this end, we first derive a closed-form expression for the MSE in image estimation. Then, we perform a min-max operation to minimize the MSE over the illumination signal by considering the maximum value for the scattering coefficients characterizing the ROI, hence determining the most effective illumination signal to employ at the transmitter.
- *RIS Configuration Design:* We extend our model to incorporate the presence of a passive RIS enabling monostatic imaging in NLOS situations between the transmitter/receiver and the ROI ("*see around the corner*"). We investigate the optimal RIS configuration maximizing the DoF of the cascade channel between the transmitting/receiving antenna, RIS, and the ROI, thereby maximizing the total cascade channel's gain and reducing the MSE of the image estimate. Moreover, we derive a closed-form expression for the optimal RIS phase profile configuration for performing imaging in the absence of visibility between the transmitter and the ROI.
- *Numerical Analysis:* We corroborate the theoretical findings through numerical simulations investigating the interplay between the DoF of the near-field illuminating and sensing channels, the geometry of the system (monostatic vs. bistatic configuration), the illumination optimization strategy, the RIS configuration, the image estimation accuracy, and image complexity. We show how the performance can be significantly improved when the number of DoF of the channel is larger than the dimensionality of the image and a suitable illuminating waveform is employed. Moreover, results indicate that optimization of the illuminating signal is effective only when the transmitting antenna is in strong near-field conditions with respect to the ROI. Finally, we demonstrate that imaging is possible in NLOS only when the RIS is optimally configured.

The paper is organized as follows. Section II introduces the system model for holographic imaging. In Section III, we discuss the ISP analytical formulation and feasible relaxation techniques, while Section IV deals with the optimization of the transmitted illuminating signal in LOS configurations. Section V extends the presented analysis to the case of a RIS-aided system working in NLOS, and Section VI illustrates the obtained numerical results. Finally, Section VII concludes the paper.

*Notation:* Throughout the paper, we use the following notation. Lowercase bold variables, e.g.,  $\mathbf{x}$ , denote vectors in the three-dimensional (3D) space. Boldface capital letters denote matrices, e.g.,  $\mathbf{X}$ . The identity and zero matrices with size  $N \times M$  are written as  $\mathbf{I}_{N \times M}$  and  $\mathbf{0}_{N \times M}$ . The transpose operator is indicated by  $(\cdot)^T$ , the Hermitian operator is  $(\cdot)^H$ , and the Moore-Penrose pseudoinverse operator is represented by  $(\cdot)^\dagger$ . The  $\mathcal{L}_2$ -norm of a vector  $\mathbf{r}$  is  $\|\mathbf{r}\|$ , the Frobenius norm of a

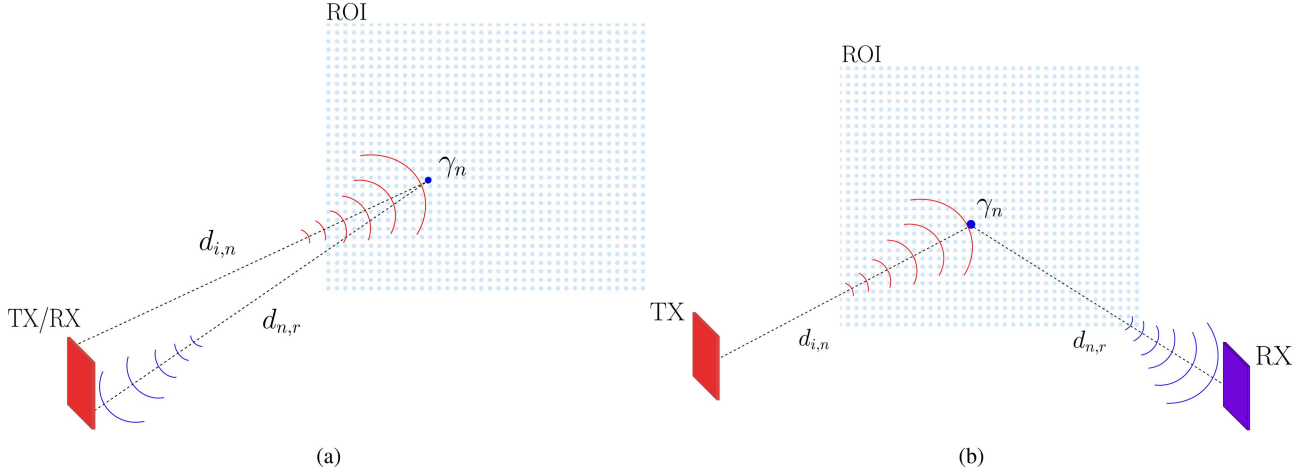


Fig. 1. (a) Monostatic configuration with a single XL-MIMO transceiver (TX/RX) performing LOS imaging of a ROI. The generic target scattering point is indicated with  $\gamma_n$ . The distances between the XL-MIMO transceiver elements and the scattering points are indicated with  $d_{i,n}$  and  $d_{n,r}$ . (b) Bistatic setup, where the transmitting antenna (TX) illuminates the selected ROI and a distinct receiving antenna (RX) collects the scattered EM signal. Both the TX and RX are modelled as XL-MIMO arrays.

matrix  $\mathbf{X}$  is  $\|\mathbf{X}\|_{\mathbb{F}}$ , and  $j$  is the imaginary unit. Calligraphic fonts are used to denote sets, i.e.,  $\mathcal{X}$ , while  $\mathbf{x} \sim \mathcal{CN}(\boldsymbol{\mu}, \boldsymbol{\Sigma})$  is a complex random vector distributed according to a complex normal distribution with mean vector  $\boldsymbol{\mu}$  and covariance matrix  $\boldsymbol{\Sigma}$ . The notation  $\text{diag}(\mathbf{x})$  denotes an operator that generates a diagonal matrix whose main diagonal is given by the vector  $\mathbf{x}$ . Finally,  $\sigma_1(\mathbf{A}) \geq \sigma_2(\mathbf{A}) \geq \dots \geq \sigma_K(\mathbf{A})$  denote the singular values of the matrix  $\mathbf{A} \in \mathbb{C}^{N \times M}$ , where  $K = \min(N, M)$ .

## II. SYSTEM MODEL

Consider a holographic imaging system as illustrated in Fig. 1. We discuss three distinct configurations: (i) a *monostatic setting* (depicted in Fig. 1(a)), wherein the transmitting and receiving discrete antenna arrays are collocated and are in a free-space LOS condition in relation to the ROI;<sup>1</sup> (ii) a *bistatic setting* (depicted in Fig. 1(b)), where the two XL-MIMO antennas are spatially separated while still maintaining LOS with the ROI under investigation; (iii) a *RIS-aided monostatic* scenario in NLOS condition (shown in Fig. 2). Specifically, with NLOS, we here refer to the case where the direct path between the XL-MIMO transceiver and the ROI to be imaged is obstructed, whereas there exists a free-space LOS condition between the RIS and both the ROI and the transceiver. In this manner, we consider that the overall XL-MIMO transceiver-ROI link is a concatenation of two free-space LOS channels connected through the RIS. The latter scenario with the RIS will be discussed in Section V while, in the sequel of this section, we will focus on the first two configurations.

The transmitting antenna array (TX) is composed of  $N_T$  antenna elements located at  $\mathbf{p}_{T,i} = [x_{T,i}, y_{T,i}, z_{T,i}]^T$ , with  $i \in \mathcal{N}_T = \{1, 2, \dots, N_T\}$ , and illuminates the ROI with a signal having wavelength  $\lambda$ . The ROI is observed by a receiving antenna array (RX) equipped with  $N_R$  antenna elements,

<sup>1</sup>Throughout the remainder of the paper, *LOS imaging* will henceforth denote the imaging procedure conducted under free-space LOS conditions.

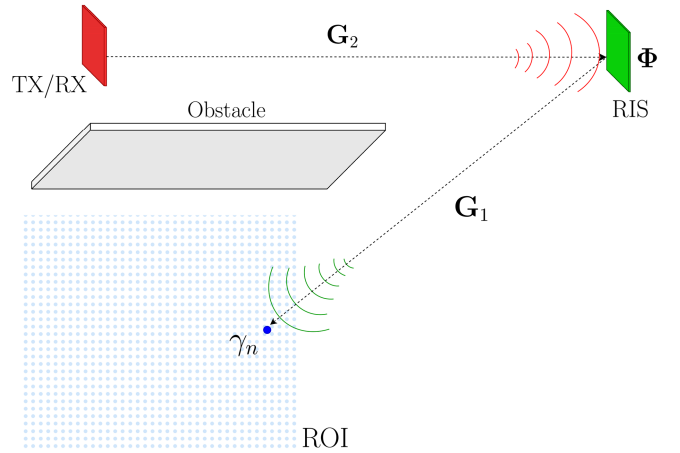


Fig. 2. Monostatic RIS-aided setup for NLOS imaging of a ROI, where the XL-MIMO transceiver (TX/RX) illuminates the RIS, the RIS reflects the impinging EM signal toward the ROI which reflects it back towards the RIS and the XL-MIMO transceiver. The TX/RX-RIS and RIS-ROI channels are indicated with  $\mathbf{G}_1$  and  $\mathbf{G}_2$ , and the RIS reflection matrix with  $\Phi$ .

each of them located at  $\mathbf{p}_{R,r} = [x_{R,r}, y_{R,r}, z_{R,r}]^T$ ,  $r \in \mathcal{N}_R = \{1, 2, \dots, N_R\}$ . In the *monostatic case*,  $\mathcal{N}_R = \mathcal{N}_T$  and  $\mathbf{p}_{T,i} = \mathbf{p}_{R,i}$ ,  $\forall i \in \mathcal{N}_T, \mathcal{N}_R$ . For both configurations, the positions of the transmitting and receiving arrays are considered as known.

The ROI is divided into a grid of  $N$  square cells of size  $\Delta$ , whose locations are  $\mathbf{p}_n = [x_n, y_n, z_n]^T$ , with  $n \in \mathcal{N} = \{1, 2, \dots, N\}$ . The  $n$ th cell is characterized by a scattering coefficient, denoted  $\gamma_n$ , related to the radar cross section (RCS) of the scatterer included in the cell (if any), i.e.,  $\text{RCS}_n = |\gamma_n|^2 \lambda^2 / 4\pi$ . If the cell is empty, then  $\gamma_n = 0$ . The magnitude of the scattering coefficient  $|\gamma_n|$  is upper bounded by the maximum RCS from a scatterer of area  $\Delta^2$ , which corresponds to the RCS of a perfect electric conductor (PEC) having the same area given by  $\text{RCS}_{\max} = \frac{4\pi}{\lambda^2} \Delta^2$ . Therefore,  $|\gamma_n| \leq \gamma_{\max} = \sqrt{\frac{4\pi}{\lambda^2} \text{RCS}_{\max}}$ ,  $\forall n \in \mathcal{N}$ .

The values of the scattering coefficients are unknown and should be estimated by the imaging process. Let us define  $\gamma = [\gamma_1, \gamma_2, \dots, \gamma_N]^T \in \mathbb{C}^{N \times 1}$  as the unknown vector, i.e., the state vector, associated with the selected ROI [62]. In the following, we assume that each scattering cell performs a perfect isotropic reflection of the illumination signal, as assumed in most of the existing literature [62].<sup>2</sup>

The TX antenna emits an illumination signal  $\mathbf{x} = [x_1, x_2, \dots, x_i, \dots, x_{N_T}]^T \in \mathbb{C}^{N_T \times 1}$ , with  $\|\mathbf{x}\|^2 \leq P_T$  and  $P_T$  the available transmit power. At the RX antenna side, the received signal  $\mathbf{y} = [y_1, y_2, \dots, y_r, \dots, y_{N_R}]^T$  is expressed as

$$\mathbf{y} = \mathbf{G}_R \mathbf{\Gamma} \mathbf{G}_T \mathbf{x} + \mathbf{w}, \quad (1)$$

where  $\mathbf{w} \in \mathbb{C}^{N_R \times 1} \sim \mathcal{CN}(0, \sigma^2 \mathbf{I}_{N_R})$  is an additive white Gaussian noise (AWGN) noise vector, whose elements are independent, identically distributed (i.i.d.) complex Gaussian random variables and  $\sigma^2$  is the noise variance. Moreover, we define

$$\mathbf{\Gamma} = \text{diag}(\gamma) = \text{diag}(\gamma_1, \gamma_2, \dots, \gamma_N) \in \mathbb{C}^{N \times N} \quad (2)$$

as the diagonal matrix containing the ROI's scattering coefficients. Finally,  $\mathbf{G}_T = \{g_{T,n,i}\} \in \mathbb{C}^{N \times N_T}$  and  $\mathbf{G}_R = \{g_{R,r,n}\} \in \mathbb{C}^{N_R \times N}$  denote, respectively, the TX-ROI and ROI-RX channel matrices. In our study, we assume that the channel is known as typical for imaging problems. We consider the performance under Rice fading propagation conditions in Section VI-C. Further information for acquiring channel state information (CSI) can be found [64], [65], [66], [67]. In the presence of RIS,  $\mathbf{G}_T$  and  $\mathbf{G}_R$  denote the cascade channels for establishing a LOS link between the TX/RX and the ROI, as further detailed in Section V.

In the following, we assume that the ROI is located in the radiative near-field region of the TX and the RX, and/or the RIS, when the distance between the ROI and the transceiver/RIS is

$$2D\sqrt{2N} \leq d \leq \frac{2(D\sqrt{2N})^2}{\lambda}, \quad (3)$$

where  $d$  is the distance between the array/RIS and the ROI,  $D$  is the size of the largest ROI/array, and  $N$  is the number of antenna elements composing the array or, equivalently, the number of ROI's pixels. This definition is the array equivalent of the Fresnel region of an antenna [68], which allows us to identify the spatial region where both the amplitude and phase variations of the EM spherical wavefronts cannot be neglected when comparing local phases between antenna elements, even if the wave is locally planar at each antenna. This corresponds to a region where we are not in a strongly near-field condition, i.e., almost close to the reactive near-field behaviors, nor in an almost far-field condition, where only phase variations among antenna elements are perceivable without amplitude variations.

In Sections III–IV we discuss LOS imaging, and NLOS imaging in Section V.

<sup>2</sup>Thanks to the adoption of high frequencies, we neglect the presence of any diffusive or multiple scattering effects. Moreover, we assume no coupling occurs between the TX/RX antennas and the scatterers.

### III. LOS IMAGING: PROBLEM FORMULATION

The primary objective of the imaging procedure is to estimate the scattering coefficient  $\gamma$  starting from the received signal in (1). To do so, we determine the best illumination signal  $\mathbf{x}$  that minimizes the estimation error with respect to  $\gamma$ . In the following, we first focus on the LOS imaging case. In Section V, we treat the NLOS RIS-aided scenario.

For LOS imaging, we can rewrite (1) as

$$\mathbf{y} = \mathbf{G}_R \mathbf{\Gamma} \tilde{\mathbf{x}} + \mathbf{w} = \mathbf{G}_R \tilde{\mathbf{X}} \boldsymbol{\gamma} + \mathbf{w}, \quad (4)$$

where  $\tilde{\mathbf{X}} = \text{diag}(\tilde{\mathbf{x}}) \in \mathbb{C}^{N \times N}$ , with  $\tilde{\mathbf{x}} = \mathbf{G}_T \mathbf{x} \in \mathbb{C}^{N \times 1}$  being the vector describing the illumination signal as observed at the ROI side. In LOS conditions, the elements of the channel matrices  $\mathbf{G}_T$  and  $\mathbf{G}_R$  in (1) and (4) are given by

$$g_{T,n,i} = \frac{\lambda}{4\pi d_{i,n}} \sqrt{G_T(\boldsymbol{\Theta}_{i,n})} e^{-j\frac{2\pi}{\lambda} d_{i,n}} \quad (5)$$

$$g_{R,r,n} = \frac{\lambda}{4\pi d_{n,r}} \sqrt{G_R(\boldsymbol{\Theta}_{n,r})} e^{-j\frac{2\pi}{\lambda} d_{n,r}}, \quad (6)$$

where  $\{n, i, r\}$  are, respectively, the  $n$ th cell of the ROI, the  $i$ th element of the TX array, and the  $r$ th element of the RX array. The quantities

$$[d_{i,n}, \boldsymbol{\Theta}_{i,n}] = [d_{i,n}, \phi_{i,n}, \theta_{i,n}], \quad (7)$$

$$[d_{n,r}, \boldsymbol{\Theta}_{n,r}] = [d_{n,r}, \phi_{n,r}, \theta_{n,r}] \quad (8)$$

represent the distance and angles between the  $(\mathbf{p}_{T,i}, \mathbf{p}_n)$  and  $(\mathbf{p}_n, \mathbf{p}_{R,r})$  pairs of TX/RX antennas and cell location. Moreover,  $\{G_T(\boldsymbol{\Theta}_{i,n}), G_R(\boldsymbol{\Theta}_{n,r})\}$  are the transmitting and receiving beam-pattern gains, evaluated in the direction of arrival (i.e.,  $\boldsymbol{\Theta}_{n,r}$ ) and departure (i.e.,  $\boldsymbol{\Theta}_{i,n}$ ). The received signal model accounts for the near-field propagation regime by considering the exact distances and angles at each antenna pair.

To decouple the estimation problem with that of the illumination design, we denote by  $\boldsymbol{\beta} = \tilde{\mathbf{X}}\boldsymbol{\gamma} \in \mathbb{C}^{N \times 1}$  the signal backscattered by the scatterers present within the ROI. As a consequence, the received signal in (4) can be rewritten as

$$\mathbf{y} = \mathbf{G}_R \boldsymbol{\beta} + \mathbf{w}, \quad (9)$$

which appears as a conventional linear estimation problem.

In the following, we discuss a possible approach for estimating the parameter vector  $\boldsymbol{\beta}$  and, thus, the scattering coefficients  $\boldsymbol{\gamma}$ . Given that the matrix  $\mathbf{G}_R$  can be rank-deficient and create ill-posed problems, we introduce truncated singular value decomposition (TSVD) regularization of the  $\mathbf{G}_R$  matrix. Subsequently, we analyze its associated MSE, which constitutes the objective function targeted for minimization in relation to the transmitted signal.

#### A. Scattering Coefficients Estimate

To determine an estimate of  $\boldsymbol{\beta}$  from (9), we consider a least squares (LS) estimator

$$\hat{\boldsymbol{\beta}} = \mathbf{G}_R^\dagger \mathbf{y} = \mathbf{G}_R^\dagger \mathbf{G}_R \boldsymbol{\beta} + \mathbf{G}_R^\dagger \mathbf{w}, \quad (10)$$

where  $\hat{\boldsymbol{\beta}}$  is the LS estimate of  $\boldsymbol{\beta}$  for  $N_R \geq N$ . To provide an expression for  $\mathbf{G}_R^\dagger$ , we first introduce the singular value

decomposition (SVD) of  $\mathbf{G}_R$ , which can be expressed as

$$\mathbf{G}_R = \mathbf{U} \mathbf{\Sigma} \mathbf{V}^H = \sum_{k=1}^K \xi_k \mathbf{u}_k \mathbf{v}_k^H, \quad (11)$$

where

$$\mathbf{\Sigma} = \begin{bmatrix} \text{diag}(\xi_1, \dots, \xi_K) & \mathbf{0}_{K \times (N-K)} \\ \mathbf{0}_{(N_R-K) \times K} & \mathbf{0}_{(N_R-K) \times (N-K)} \end{bmatrix} \in \mathbb{C}^{N_R \times N} \quad (12)$$

is a diagonal matrix with  $K = \min(N_R, N)$  diagonal elements  $\xi_k = \sigma_k(\mathbf{G}_R) \in \mathbb{R}_0^+$ ,  $\mathbb{R}_0^+ = [0, +\infty)$ ,  $k \in \mathcal{K} = \{1, \dots, K\}$ , and where  $\mathbf{U} \in \mathbb{C}^{N_R \times N_R}$  and  $\mathbf{V} \in \mathbb{C}^{N \times N}$  are unitary matrices, with  $\mathbf{u}_k$  and  $\mathbf{v}_k$  being the columns of  $\mathbf{U}$  and  $\mathbf{V}$  respectively, i.e., the left-singular vectors and right-singular vectors of  $\mathbf{G}_R$ .

The SVD of  $\mathbf{G}_R^\dagger$  is given by [69], [70]

$$\mathbf{G}_R^\dagger = \mathbf{V} \mathbf{\Sigma}^\dagger \mathbf{U}^H = \sum_{k=1}^K \xi_k^{-1} \mathbf{v}_k \mathbf{u}_k^H, \quad (13)$$

with  $\mathbf{G}_R^\dagger \in \mathbb{C}^{N \times N_R}$  and  $\mathbf{\Sigma}^\dagger \in \mathbb{C}^{N \times N_R}$ . In our specific case, the multiple-input multiple-output (MIMO) wireless channel, represented by the matrix  $\mathbf{G}_R$ , typically does not possess full rank. Therefore, the presence of null or very small eigenvalues  $\xi_k$  within the matrix  $\mathbf{\Sigma}$  poses challenges in computing its pseudoinverse, thus leading to numerical instability [25], [71]. To address this issue, a typical approach is to introduce regularization resulting in [25]

$$\mathbf{\Sigma} \approx \tilde{\mathbf{\Sigma}} = \begin{bmatrix} \text{diag}(\omega_1 \xi_1, \dots, \omega_K \xi_K) & \mathbf{0}_{K \times (N-K)} \\ \mathbf{0}_{(N_R-K) \times K} & \mathbf{0}_{(N_R-K) \times (N-K)} \end{bmatrix}, \quad (14)$$

where  $\{\omega_1, \omega_2, \dots, \omega_K\}$  are weights used by the regularization technique, e.g., TSVD [56] or Tikhonov [72].

Then, by denoting the pseudoinverse of (14) as  $\tilde{\mathbf{\Sigma}}^\dagger$ , we have

$$\tilde{\mathbf{G}}_R^\dagger = \mathbf{V} \tilde{\mathbf{\Sigma}}^\dagger \mathbf{U}^H = \sum_{k=1}^K \omega_k^{-1} \xi_k^{-1} \mathbf{v}_k \mathbf{u}_k^H. \quad (15)$$

Therefore,  $\hat{\boldsymbol{\beta}}$  can be computed as

$$\hat{\boldsymbol{\beta}} = \mathbf{V} \tilde{\mathbf{\Sigma}}^\dagger \mathbf{U}^H \mathbf{y} = \mathbf{V} \tilde{\mathbf{\Sigma}}^\dagger \mathbf{\Sigma} \mathbf{V}^H \boldsymbol{\beta} + \mathbf{z} = \mathbf{V} \mathbf{\Lambda} \mathbf{V}^H \boldsymbol{\beta} + \mathbf{z}, \quad (16)$$

where  $\mathbf{z} = \tilde{\mathbf{G}}_R^\dagger \mathbf{w} = \mathbf{V} \tilde{\mathbf{\Sigma}}^\dagger \mathbf{U}^H \mathbf{w}$ , and  $\mathbf{\Lambda} = \tilde{\mathbf{\Sigma}}^\dagger \mathbf{\Sigma} \in \mathbb{C}^{N \times N}$  is a diagonal matrix with its first  $K$  elements different from zero and the remaining  $(N - K)$  elements are null, i.e.,

$$\mathbf{\Lambda} = \text{diag}(\omega_1^{-1}, \omega_2^{-1}, \dots, \omega_K^{-1}, 0, \dots, 0). \quad (17)$$

Defining  $\mathbf{H} = \mathbf{V} \mathbf{\Lambda} \mathbf{V}^H \in \mathbb{C}^{N \times N}$ , we obtain

$$\begin{aligned} \hat{\boldsymbol{\beta}} &= \mathbf{H} \boldsymbol{\beta} + \mathbf{z} = \mathbf{H} \tilde{\mathbf{X}} \boldsymbol{\gamma} + \mathbf{z} = \mathbf{H} \text{diag}(\mathbf{G}_T \mathbf{x}) \boldsymbol{\gamma} + \mathbf{z} \\ &= \boldsymbol{\beta} + (\mathbf{H} - \mathbf{I}) \text{diag}(\tilde{\mathbf{x}}) \boldsymbol{\gamma} + \mathbf{z}. \end{aligned} \quad (18)$$

Assume that  $\tilde{\mathbf{X}}$  is a full-rank square diagonal matrix, i.e.,  $\tilde{\mathbf{x}}$  does not contain zero elements, which is generally reasonable. Then, we can easily obtain an estimate of  $\boldsymbol{\gamma}$  from  $\hat{\boldsymbol{\beta}}$  by multiplying both sides of (18) by  $\tilde{\mathbf{X}}^{-1}$ , leading to

$$\hat{\boldsymbol{\gamma}} = \boldsymbol{\gamma} + \tilde{\mathbf{X}}^{-1} (\mathbf{H} - \mathbf{I}) \tilde{\mathbf{X}} \boldsymbol{\gamma} + \tilde{\mathbf{X}}^{-1} \mathbf{z}. \quad (19)$$

We can identify three distinct terms contributing to the LS estimate  $\hat{\boldsymbol{\gamma}}$ : (i) the true original value of the estimated quantity (i.e.,  $\boldsymbol{\gamma}$ ); (ii) a distortion term due to the regularization process (i.e.,  $\tilde{\mathbf{X}}^{-1} (\mathbf{H} - \mathbf{I}) \tilde{\mathbf{X}} \boldsymbol{\gamma}$ ); and (iii) the noise contribution (i.e.,  $\tilde{\mathbf{X}}^{-1} \mathbf{z}$ ).

### B. Mean Squared Error

To evaluate the accuracy in estimating  $\boldsymbol{\gamma}$ , we now derive a closed-form expression for the MSE. Let us start by defining the covariance matrix  $\mathbf{C} \in \mathbb{C}^{N \times N}$  of the error vector  $(\boldsymbol{\gamma} - \hat{\boldsymbol{\gamma}})$

$$\begin{aligned} \mathbf{C} &= \mathbb{E} \{ (\boldsymbol{\gamma} - \hat{\boldsymbol{\gamma}}) (\boldsymbol{\gamma} - \hat{\boldsymbol{\gamma}})^H \} \\ &= \mathbb{E} \left\{ \left( \tilde{\mathbf{X}}^{-1} (\mathbf{H} - \mathbf{I}) \tilde{\mathbf{X}} \boldsymbol{\gamma} + \tilde{\mathbf{X}}^{-1} \mathbf{z} \right) \right. \\ &\quad \left. \times \left( \tilde{\mathbf{X}}^{-1} (\mathbf{H} - \mathbf{I}) \tilde{\mathbf{X}} \boldsymbol{\gamma} + \tilde{\mathbf{X}}^{-1} \mathbf{z} \right)^H \right\}. \end{aligned} \quad (20)$$

Let us assume that the only random vector is  $\mathbf{z}$  and consider  $\boldsymbol{\gamma}$  as an unknown deterministic vector. After some computations, reported in Appendix A, the MSE as a function of the signal  $\tilde{\mathbf{x}}$  can be calculated as the trace of the covariance matrix  $\mathbf{C}$ , resulting in

$$\begin{aligned} \text{MSE}(\boldsymbol{\gamma}; \tilde{\mathbf{x}}) &= \text{tr}(\mathbf{C}) \\ &= \sum_{n=1}^N \left| (h_{n,n} - 1) \gamma_n + \tilde{x}_n^{-1} \sum_{\substack{i=1 \\ i \neq n}}^N h_{n,i} \tilde{x}_i \gamma_i \right|^2 \\ &\quad + \sum_{n=1}^N \frac{\sigma^2}{|\tilde{x}_n|^2} \sum_{k=1}^K \omega_k^{-2} \xi_k^{-2} |v_{n,k}|^2, \end{aligned} \quad (21)$$

where  $h_{n,i}$  are the elements of  $\mathbf{H}$  and  $v_{n,k}$  are the elements of the vector  $\mathbf{v}_k$ . In (21), it is possible to identify two distinct contributions: the first addend is the distortion in the estimation procedure introduced by the regularization technique, whereas the second term is associated with the AWGN noise.

Notably, (21) depends on  $\boldsymbol{\gamma}$ , which is the objective of the estimation process and depends on the physical scatterers present within the ROI, thus being unmodifiable. At the same time, the MSE depends on the illumination signal  $\mathbf{x}$ , and varying  $\mathbf{x}$  might lead to different levels of estimation accuracy (i.e., of distinct values of MSE). For this reason, in the sequel, we formulate an optimization problem aimed at minimizing the MSE across the vector  $\mathbf{x}$ , while simultaneously constraining  $\boldsymbol{\gamma}$  to its maximum value, which corresponds to the worst achievable MSE.

## IV. OPTIMIZATION OF THE ILLUMINATION SIGNAL FOR LOS IMAGING

As highlighted in the previous section, a fundamental aspect of performing imaging is to identify the optimal illumination signal  $\mathbf{x}^*$  that minimizes the MSE defined in (21). To facilitate the analysis, we decompose the problem into two subsequent steps. First, we estimate the illumination signal  $\tilde{\mathbf{x}}^* = \mathbf{G}_T \mathbf{x}^*$  that should be received at the ROI, i.e., after propagating through the TX-ROI channel  $\mathbf{G}_T$ . Secondly, we derive the corresponding transmit signal  $\mathbf{x}^*$  to enable a received illumination signal that

closely approximates  $\tilde{\mathbf{x}}^*$ . Since the MSE depends on the actual value of  $\gamma$ , which is unknown, we formulate our problem as follows

$$\begin{aligned} \tilde{\mathbf{x}}^* &= \arg \min_{\mathbf{x}} \max_{\gamma} \text{MSE}(\gamma; \tilde{\mathbf{x}}) \\ \text{s.t. } & \|\mathbf{x}\|^2 \leq P_T \\ & |\gamma_n| \leq \gamma_{\max}, n = 1, 2, \dots, N, \end{aligned} \quad (22)$$

where we recall that  $\tilde{\mathbf{x}}$  can be expressed as a function of  $\mathbf{x}$  as  $\tilde{\mathbf{x}} = \mathbf{G}_T \mathbf{x}$ , and that the maximum magnitude of the scattering coefficient is  $\gamma_{\max}$  as defined in Section II.

Given the complexity of globally solving the optimization problem described in (22) due to the dependence of the MSE on both  $\gamma$  and  $\tilde{\mathbf{x}}$ , we opt to tackle a fundamentally different analytical problem. This approximates the original optimization problem, enabling us to derive a closed-form solution, whose performance will then be compared with that achieved through numerical optimization. To this end, we first establish an upper bound of the cost function in (22). By applying the submultiplicative property, asserting that  $\|\mathbf{A}\mathbf{b}\|_F^2 \leq \|\mathbf{A}\|_F^2 \|\mathbf{b}\|_F^2$  for any matrices  $\mathbf{A}$  and  $\mathbf{b}$ , to the first term on the right hand of (21), we obtain the following inequality

$$\max_{\gamma} \text{MSE}(\gamma; \tilde{\mathbf{x}}) \leq f(\gamma_{\max}; \tilde{\mathbf{x}}) + g(\tilde{\mathbf{x}}), \quad (23)$$

which provides the upper-bound value for the  $\text{MSE}(\gamma; \tilde{\mathbf{x}})$  in regards to the unknown parameter  $\gamma$ . Specifically, this upper-bound encompasses two distinguishable terms, i.e.,  $f(\gamma_{\max}; \tilde{\mathbf{x}})$  and  $g(\tilde{\mathbf{x}})$ , which are associated, respectively, with the truncation error and the AWGN noise and given by

$$f(\gamma_{\max}; \tilde{\mathbf{x}}) = N\gamma_{\max}^2 \sum_{n=1}^N \left| (h_{n,n} - 1) + \tilde{x}_n^{-1} \sum_{\substack{i=1 \\ i \neq n}}^N h_{n,i} \tilde{x}_i \right|^2, \quad (24)$$

$$g(\tilde{\mathbf{x}}) = \sum_{n=1}^N \frac{\sigma^2}{|\tilde{x}_n|^2} \sum_{k=1}^K \omega_k^{-2} \xi_k^{-2} |v_{n,k}|^2. \quad (25)$$

According to (23), we can reformulate the problem (22) as per

$$\begin{aligned} \tilde{\mathbf{x}}^* &= \arg \min_{\mathbf{x}} f(\gamma_{\max}; \tilde{\mathbf{x}}) + g(\tilde{\mathbf{x}}) \\ \text{s.t. } & \|\mathbf{x}\|^2 \leq P_T. \end{aligned} \quad (26)$$

Due to the non-linear and non-convex nature of the objective function presented in (26), solving it directly poses a substantial challenge. To address this difficulty, we propose a two-step algorithm for its effective solution. In the first step, we temporarily ignore the term  $f(\gamma_{\max}; \tilde{\mathbf{x}})$  and focus solely on  $g(\tilde{\mathbf{x}})$ . Given this simplification, (26) can be written as follows

$$\begin{aligned} \underset{\mathbf{x}}{\text{minimize}} \quad & g(\tilde{\mathbf{x}}) = \sum_{n=1}^N \frac{\sigma^2}{|\tilde{x}_n|^2} \sum_{k=1}^K \omega_k^{-2} \xi_k^{-2} |v_{n,k}|^2 \\ \text{s.t. } & \|\mathbf{x}\|^2 \leq P_T. \end{aligned} \quad (27)$$

While still retaining its non-convex nature, it is feasible to obtain a closed-form solution for the simplified problem in (27), as validated by the following theorem.

*Theorem 1:* The optimal solution to problem (27) is given by

$$\tilde{x}_n^* = \sqrt{b_n} e^{j\phi_n}, n = 1, 2, \dots, N, \quad (28)$$

where

$$b_n = \frac{P\sqrt{\alpha_n}}{\sum_n \sqrt{\alpha_n}}, \quad (29)$$

denotes the magnitude of the optimal  $\tilde{x}_n^*$ ,  $\phi_n$  can be any arbitrary phase, and

$$\alpha_n \triangleq \sigma^2 \sum_{k=1}^K (\omega_k \xi_k)^{-2} |v_{n,k}|^2, \quad (30)$$

$$P = P_T \cdot \sum_n \mathbf{g}_{T,n} \mathbf{g}_{T,n}^H, \quad (31)$$

with  $P$  denoting the upper bound of the term  $\sum_n |\tilde{x}_n|^2$ .

*Proof:* See Appendix B.

Theorem 1 indicates that the optimal solution to problem (27) is independent of the phase of each  $\tilde{x}_n$ . This independence arises because the magnitude squared operation in (25) eliminates the phase information. Consequently, commencing with the solution  $\tilde{x}_n^* = \sqrt{b_n} e^{j\phi_n}$  obtained in the initial step, the subsequent optimization involves adjusting the phase  $\phi_n$  of each component to minimize  $f(\tilde{\mathbf{x}}, \gamma_{\max})$ , while keeping  $b_n$  fixed. Indeed, optimizing only the phase does not compromise the optimality of the solution found for  $g(\tilde{\mathbf{x}})$ . Thus, by substituting  $\tilde{x}_n^* = \sqrt{b_n} e^{j\phi_n}$  into (24), the second step entails solving the following optimization problem

$$\min_{\{\phi_n \in [0, 2\pi)\}} f(\gamma_{\max}; \{\phi_n\}), \quad (32)$$

where

$$\begin{aligned} f(\gamma_{\max}; \{\phi_n\}) \\ = N\gamma_{\max}^2 \sum_{n=1}^N \left| (h_{n,n} - 1) + \frac{e^{-j\phi_n}}{\sqrt{b_n}} \sum_{\substack{i=1 \\ i \neq n}}^N \frac{h_{n,i}}{\sqrt{b_i}} e^{-j\phi_i} \right|^2. \end{aligned} \quad (33)$$

Determining directly the optimal  $\phi_n$  for (32) is challenging due to the complexity of the absolute value operation, which introduces non-differentiable points. To overcome this, we employ an alternating optimization method, wherein we optimize each phase term  $\phi_n$  while keeping all other phases fixed. After optimizing  $\phi_n$ , we proceed to optimize  $\phi_{n+1}$ , and so forth, in an alternating manner. Specifically, for a fixed  $n$ , the optimization problem (32) can be formulated as

$$\underset{\phi_n \in [0, 2\pi)}{\text{minimize}} \left| (h_{n,n} - 1) + \frac{e^{-j\phi_n}}{\sqrt{b_n}} \sum_{\substack{i=1 \\ i \neq n}}^N h_{n,i} \frac{e^{-j\phi_i}}{\sqrt{b_i}} \right|^2. \quad (34)$$

By leveraging the geometric nature of the problem (34), its optimal solution can be expressed as

$$\phi_n^* = [\arg(d_n) - \arg(c_n) - \delta_n \pi] \bmod 2\pi, \quad (35)$$

---

**Algorithm 1:** Proposed Algorithm for Solving Problem (26).
 

---

- 1: Initialize the phase parameters  $\{\phi_n\}_{n=1}^N$ .
  - 2: Calculate  $\{b_n\}_{n=1}^N$  according to (29);
  - 3: **Repeat**
  - 4:   Update the phases  $\{\phi_n\}_{n=1}^N$  in an alternating (element-wise) manner according to (35);
  - 5: **Until** the objective function value in (32) converges.
  - 6: **Output:**  $\{\tilde{x}_n^* = \sqrt{b_n} e^{j\phi_n^*}\}_{n=1}^N$ .
- 

for  $n = 1, 2, \dots, N$ , where

$$c_n = (h_{n,n} - 1), \quad (36)$$

$$d_n = \frac{1}{\sqrt{b_n}} \sum_{\substack{i=1 \\ i \neq n}}^N h_{n,i} \frac{e^{-j\phi_i}}{\sqrt{b_i}}, \quad (37)$$

and

$$\delta_n \triangleq \begin{cases} +1 & \text{if } \arg(c_n) \in [0, \pi) \\ -1 & \text{if } \arg(c_n) \in [\pi, 2\pi). \end{cases} \quad (38)$$

The combination of (28) and (35) provides the most suitable illumination that is required at the ROI side to minimize the MSE given worst-case magnitudes for  $\gamma$ .

The proposed two-step algorithm for solving the problem in (26) is summarized as Algorithm 1, whose computational complexity is analyzed as follows. The complexity for calculating  $\{b_n\}_{n=1}^N$  is  $\mathcal{O}(N)$ . The complexity for updating  $N$  phases is  $\mathcal{O}(TN)$ , where  $T$  denotes the number of iterations required for convergence. Therefore, the overall computational complexity of Algorithm 1 is  $\mathcal{O}((T+1)N)$ .

As a final step, to obtain the corresponding illumination signal to be employed at the TX side, we compute

$$\mathbf{x}^* = \mathbf{G}_T^\dagger \tilde{\mathbf{x}}^*. \quad (39)$$

Since, in general,  $\mathbf{G}_T$  is not a full-rank matrix, the result obtained is the minimum norm solution given the limited  $N_{\text{DOF}}^{(c)}$  of the TX-ROI channel  $\mathbf{G}_T$ .

## V. RIS-AIDED NLOS IMAGING

According to the existing literature, passive walls have mostly been employed to assist the TX in conventional NLOS imaging problems [40], [54]. However, introducing a RIS allows for the design of a smarter reflection, potentially enhancing imaging performance. As illustrated in Fig. 2, we now extend the previous analysis to the case where the illuminating link ( $\mathbf{G}_T$ ) used to illuminate the target ROI and/or the sensing link ( $\mathbf{G}_R$ ), delivering the scattered EM field, is in NLOS condition and is supported by a RIS whose parameters have to be optimized.

Denote with  $\mathbf{G}$  the cascade channel of interest (therefore, it could be equally to  $\mathbf{G} = \mathbf{G}_T$  and/or  $\mathbf{G} = \mathbf{G}_R$ ). It can be decomposed into

$$\mathbf{G} = \mathbf{G}_1 \Phi \mathbf{G}_2, \quad (40)$$

where  $\mathbf{G}_2$  is the TX-RIS (RX-RIS) channel matrix,  $\mathbf{G}_1$  is the RIS-ROI matrix, and  $\Phi$  the matrix characterizing the RIS phase shifts configuration. We do not restrict  $\Phi$  to be diagonal to ensure general applicability. Given the passive and lossless nature of the RIS, it follows that  $\Phi^H \Phi = \mathbf{I}$ , indicating unitarity. The scenario in which the reflection is not attributed to the RIS but rather arises from a natural reflector, characterized by a specular reflection (e.g., a wall), can be straightforwardly represented by defining  $\Phi = \eta \mathbf{I}$ , where  $0 < |\eta| \leq 1$  denotes the reflection coefficient ( $\eta = 1$  corresponds to a PEC).

As evident from the previous analysis and the numerical results, the imaging quality depends on the rank (i.e., the DoF) of the cascade channel matrix  $\mathbf{G}$  as well as its total gain  $\|\mathbf{G}\|_F^2$ . In general, being

$$\text{rank}(\mathbf{G}_1 \Phi \mathbf{G}_2) \leq \min(\text{rank}(\mathbf{G}_1), \text{rank}(\Phi), \text{rank}(\mathbf{G}_2)), \quad (41)$$

the rank of the cascade channel is dominated by the channel with minimum rank. Since the number of elements of the RIS is typically larger than  $\text{rank}(\mathbf{G}_1)$  or  $\text{rank}(\mathbf{G}_2)$  and the RIS phase matrix is full rank, it does not concur in determining the rank of the cascade channel. More precisely, the rank of the cascade channel cannot be increased through a specific RIS design. Therefore, to improve the image quality we seek the optimal RIS's configuration  $\Phi$  which maximizes  $\|\mathbf{G}\|_F^2 = \sum_n \xi_n^2$ , where  $\xi_n = \sigma(\mathbf{G})$  are the singular values of  $\mathbf{G}$ , under the constraint  $\Phi^H \Phi = \mathbf{I}$  (passive RIS) and for fixed  $\mathbf{G}_1$  and  $\mathbf{G}_2$  matrices. To this end, we recall the following Theorem [73]:

*Theorem 2:* Given Hermitian matrices  $\mathbf{A}_1 \in \mathbb{C}^{N \times N}$ ,  $\mathbf{A}_2 \in \mathbb{C}^{N \times N}$  and  $\mathbf{A}_3 \in \mathbb{C}^{N \times N}$  with singular values, respectively,  $\sigma_n(\mathbf{A}_1)$ ,  $\sigma_n(\mathbf{A}_2)$  and  $\sigma_n(\mathbf{A}_3)$ , we have

$$\sum_n \sigma_n^2(\mathbf{A}) \leq \sum_n \sigma_n^2(\mathbf{A}_1) \sigma_n^2(\mathbf{A}_2) \sigma_n^2(\mathbf{A}_3), \quad (42)$$

where  $\mathbf{A} = \mathbf{A}_1 \mathbf{A}_2 \mathbf{A}_3$ . The equality is true when

$$\sigma_n(\mathbf{A}) = \sigma_n(\mathbf{A}_1) \sigma_n(\mathbf{A}_2) \sigma_n(\mathbf{A}_3), \quad \forall n. \quad (43)$$

Let us define

$$\mathbf{A}_1 = \mathbf{G}_1^H \mathbf{G}_1, \quad \mathbf{A}_2 = \Phi^H \Phi, \quad \mathbf{A}_3 = \mathbf{G}_2^H \mathbf{G}_2. \quad (44)$$

We perform the SVD decomposition  $\mathbf{G}_1 = \mathbf{U}_1 \Sigma_1 \mathbf{V}_1^H$  and  $\mathbf{G}_2 = \mathbf{U}_2 \Sigma_2 \mathbf{V}_2^H$ . Since  $\mathbf{A}_2 = \Phi^H \Phi = \mathbf{I}$ , the right hand side of (42) does not depend on the RIS's configuration  $\Phi$  and hence achieving the equality in (42) ensures that  $\sum_n \sigma_n^2(\mathbf{A})$  is maximized. We can thus write

$$\mathbf{G} = \mathbf{U}_1 \Sigma_1 \mathbf{V}_1^H \Phi \mathbf{U}_2 \Sigma_2 \mathbf{V}_2^H. \quad (45)$$

Let us now define  $\Phi = \mathbf{V}_1 \mathbf{Z} \mathbf{U}_2^H$ , with  $\mathbf{Z}$  being a generic unitary matrix. Then, we can rewrite (45) as

$$\mathbf{G} = \mathbf{U}_1 \Sigma_1 \mathbf{Z} \Sigma_2 \mathbf{V}_2^H = \mathbf{U}_1 \Sigma_t \mathbf{V}_2^H, \quad (46)$$

having defined the matrix  $\Sigma_t = \Sigma_1 \mathbf{Z} \Sigma_2$ . Note that  $\Sigma_t$  is in general not diagonal because of  $\mathbf{Z}$ .

If we choose  $\mathbf{Z} = \mathbf{I}$ ,  $\Sigma_t$  becomes diagonal and (46) takes the form of the SVD of the matrix  $\mathbf{G}$ . As a consequence, in (42)

it is  $\sigma_n^2(\mathbf{A}) = \sigma_n^2(\mathbf{A}_1) \sigma_n^2(\mathbf{A}_3)$ ,  $\forall n$ , being  $\sigma_n^2(\mathbf{A}_2) = 1$ . This translates in

$$\xi_n^2 = \sigma_n^2(\mathbf{G}) = \sigma_n^2(\mathbf{G}_1) \sigma_n^2(\mathbf{G}_2), \quad \forall n, \quad (47)$$

by considering that  $\sigma_n^2(\Phi) = 1$  being  $\Phi$  unitary. According to Theorem 2, we obtain the equality in (42), thus maximizing the quantity  $\sum_n \xi_n^2$ . As a result, the optimal RIS configuration is given by

$$\Phi = \mathbf{V}_1 \mathbf{U}_2^H. \quad (48)$$

Incidentally, this is the same result achieved in [74] through an alternative method for maximizing the mutual information between a TX and a RX communicating via a RIS. Note that, in general, the optimal  $\Phi$  configuration is not in a diagonal form.

## VI. NUMERICAL RESULTS

### A. Simulation Setup

In the proposed setup, imaging is performed over a narrow frequency band  $\Delta f = 120$  kHz centered at  $f_c = 28$  GHz, with a wavelength of  $\lambda \simeq 0.01$  m. This choice can correspond to adopting a sub-carrier or a resource block in a orthogonal frequency division multiplexing (OFDM) signal used also for communication. We set the noise power spectral density to  $\sigma^2 = -170$  dBm/Hz, and the transmitted power  $P_T$  to 30 dBm. The XL-MIMO TX and RX arrays are configured as uniform squared arrays with the same size of  $(10\lambda \times 10\lambda) \text{ m}^2$ , with antenna elements spaced apart of  $\lambda/2$  (i.e.,  $20 \times 20$  antennas in the considered settings). The ROI spans dimensions of  $(750\lambda \times 750\lambda) \text{ m}^2$ , with  $8 \times 8$  cells equally distributed with an inter-spacing of  $\Delta = 93.75\lambda$ , if not otherwise indicated. In the simulations, in the presence of a scatterer in the  $n$ th cell,  $\gamma_n$  has been set equal to  $M = 10^{-1} \gamma_{\max}$  because, in realistic scenarios, objects typically exhibit a RCS smaller than those observed in the case of a PEC. Specifically, the magnitude of the scattering coefficients  $\gamma$ , i.e., the image, to be estimated is depicted in Fig. 4-(top,left). When present, the RIS has dimensions equal to  $(60\lambda \times 60\lambda) \text{ m}^2$  and is in paraxial configuration with respect to the TX/RX. The RIS's elements are separated by a distance equal to  $\lambda/2$  (i.e.,  $120 \times 120$  RIS elements in the setup in Fig. 2).

For each simulation, we evaluated both the empirical and theoretical MSE together with its normalized mean squared error (NMSE) version. These metrics are computed as

$$\text{E-MSE} = \frac{\sum_{m=1}^{N_{\text{MC}}} \|\gamma - \hat{\gamma}_m\|^2}{N_{\text{MC}}}, \quad \text{E-NMSE} = \frac{\text{E-MSE}}{NM^2}, \quad (49)$$

where  $N_{\text{MC}}$  represents the number of Monte Carlo iterations that were set to 100. Likewise, the theoretical MSE (T-MSE) is given by (21) and its normalized version is denoted with T-NMSE. Notably, the relationship between the peak signal to noise ratio (PSNR) and NMSE is expressed as  $\text{PSNR} = \text{NMSE}^{-1}$ .<sup>3</sup> In our results, the following cases were considered:

- *No regularization, No optimization (NO REG-NO OPT)*: This represents the worst-case scenario, where we considered neither the  $\mathbf{G}_R$  matrix regularization nor the optimization of the transmit illuminating vector. This scenario is incorporated in our simulations as a benchmark. In the following cases,  $\mathbf{G}_R$  regularization is always performed.
- *Regularization, No optimization (NO OPT)*: In this case, we considered the regularization of the matrix  $\mathbf{G}_R$  but we did not apply the optimization of the transmitting signal, setting it equal to  $\mathbf{x} = \frac{\sqrt{P_T}}{2N_T} (\mathbf{1}_{N_T \times 1} + j\mathbf{1}_{N_T \times 1})$ . This choice corresponds to a uniform ROI illumination.
- *Uniform Interior-Point Optimization (U-IP-OPT)*: We applied the optimization of the transmitting vector by running an interior-point method [75] to search for  $\tilde{\mathbf{x}}^*$  starting from a guess solution equal to  $\tilde{\mathbf{x}}_0 = \frac{\sqrt{P_T}}{2N_T} \mathbf{G}_T (\mathbf{1}_{N_T \times 1} + j\mathbf{1}_{N_T \times 1})$  and  $\gamma^* = \gamma_{\max} \mathbf{1}_{N \times 1}$ . To compute the transmitted vector, we applied  $\mathbf{x}^* = \tilde{\mathbf{G}}_T^\dagger \tilde{\mathbf{x}}^*$ , with  $\tilde{\mathbf{G}}_T$  being the regularized version of  $\mathbf{G}_T$ .
- *Analytical Solution (A-OPT)*: In this case, we applied the optimization of the transmitting vector by implementing (28) with  $\gamma^* = \gamma_{\max} \mathbf{1}_{N \times 1}$ . Then, as before, to derive the transmitted vector, we applied  $\mathbf{x}^* = \tilde{\mathbf{G}}_T^\dagger \tilde{\mathbf{x}}^*$ .
- *Analytical Interior-Point Optimization (A-IP-OPT)*: It is the same approach as U-IP-OPT but with a different initial guess  $\tilde{\mathbf{x}}_0$ , which is set equal to the analytical solution in (28).

Notably, the number of DoF associated with the wireless channel, particularly  $\mathbf{G}_R$ , impacts the imaging accuracy and the capability of estimating the scattering features of the ROI. Specifically, recalling the results obtained in [10, Eq. 31], it can be shown that

$$N_{\text{DOF}}^{(c)} \simeq \frac{2L^2}{\lambda^2} \times \left( \frac{S \cdot \tan^{-1} \left( \frac{S}{\sqrt{4d^2 + S^2}} \right)}{\sqrt{4d^2 + S^2}} + \frac{S \cdot \tan^{-1} \left( \frac{S}{\sqrt{4d^2 + S^2}} \right)}{\sqrt{4d^2 + S^2}} \right), \quad (50)$$

where  $L = L_x = L_y$  denotes the side of the device having the smallest area, e.g., the TX/RX,  $S = S_x = S_y$  denotes the side of the larger entity, i.e., the ROI, and  $d$  represents the distance between their centers. Such a number approximates the rank of the channel matrix of the considered link. Particularly, the geometric setup is favorable for holographic imaging if it is close to  $K = \min(N_R, N)$ , i.e.,  $N_{\text{DOF}}^{(c)} \rightarrow K$ . This also hints that no regularization is required to estimate  $\gamma$  if the channel matrices are full-rank. Conversely, as the number of DoF diminishes (with the far-field condition representing the most challenging scenario, wherein  $N_{\text{DOF}}^{(c)} = 1$ ), there is a substantial deterioration in the imaging performance. In such cases, regularization is pivotal in facilitating the resolution of the ill-posed ISP. Nevertheless, the imaging performance is influenced not only by  $N_{\text{DOF}}^{(c)}$  but also by the complexity of the image. A rough estimate of such complexity could be given by the number of the most significant principal components, denoted as  $N_{\text{DOF}}^{(i)}$ , derived using the principal component analysis (PCA) [76]. Through simulations, we will explore the interplay between these two quantities.

<sup>3</sup>The PSNR, a commonly utilized metric in image processing, denotes the ratio between the maximum attainable power of the generic pixel and the power of the estimation noise influencing the fidelity of its representation [36].



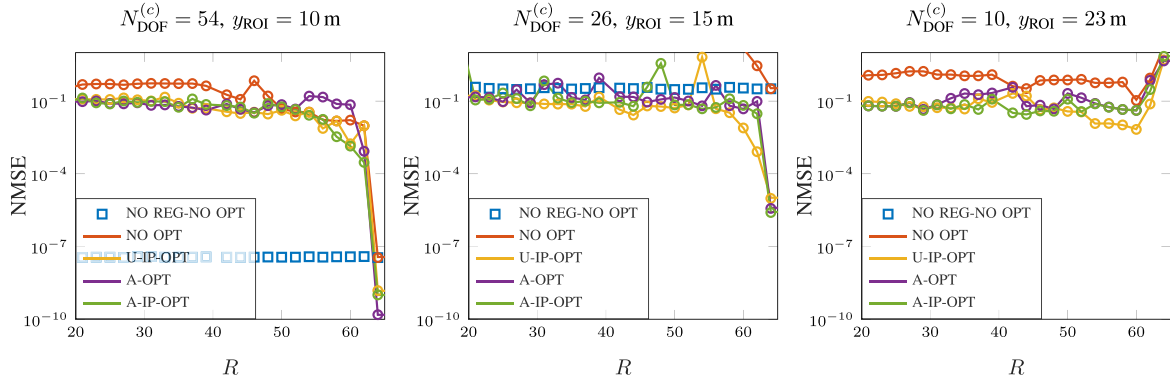


Fig. 3. NMSE as a function of the truncation index  $R$  selected when applying the TSVD to  $\mathbf{G}_R$  and different optimization techniques for the monostatic LOS setup. The TX/RX XL-MIMO array is located at  $(0, 0, 0)$  m and three distinct locations for the ROI are tested, namely  $y_{\text{ROI}} \in \{10, 15, 23\}$  m. Dotted ( $\circ$ ) and continuous ( $-$ ) lines correspond to the E-NMSE and T-NMSE, respectively, while the square markers denote the non-regularized case for benchmarking.

To investigate the impact of regularization on the imaging performance, we employ a TSVD approach with a fixed threshold to retain only the first  $R$  eigenvalues of  $\mathbf{G}_R$ . Conversely, in the case of the  $\mathbf{G}_T$  matrix, we adopt TSVD by retaining all eigenvalues whose cumulative sum does not surpass 99% of the total transmit power  $P_T$ , being the illuminating channel not subject to any noise enhancement.

### B. Monostatic LOS Imaging Performance

Let us consider a monostatic LOS configuration as per Fig. 1(a), with the center of the TX/RX array set in  $(0, 0, 0)$  m and the ROI center in  $(0, y_{\text{ROI}}, 0)$  m, with  $y_{\text{ROI}} \in \{10, 15, 23\}$  m. These distances correspond to different channel DoF, i.e.,  $N_{\text{DOF}}^{(c)} \in \{54, 26, 10\}$ , evaluated as per (50).

In Fig. 3, the curves depicting the E-NMSE and T-NMSE are presented for different values of the selected truncation index  $R$ , with  $R \leq K$ . In this setup, it is  $K = N = 64$ . Let us analyze this figure from left to right, progressing from a strong near-field to an almost far-field regime as the link distance between the TX/RX and the ROI increases. Fig. 3-left corresponds to a specific scenario where regularization is unnecessary due to the full-rank nature of the channel matrix  $\mathbf{G}_R$ , resulting in good imaging performance ( $N_{\text{DOF}}^{(c)} = 54$ ). Similarly, as shown in Fig. 3-center, this geometric configuration still yields quite satisfactory imaging performance even in the absence of regularization and/or optimization. This outcome is attributed to the specific  $N_{\text{DOF}}^{(i)}$  of the image evaluated through PCA as specified above. Indeed, for the L-shaped image of Fig. 4-(top, left),  $N_{\text{DOF}}^{(i)} = 2$ , and hence, since  $N_{\text{DOF}}^{(c)} \gg N_{\text{DOF}}^{(i)}$ , regularization is unnecessary. Consequently, for truncation indices  $R < N$ , a decline in performance is observed for all the cases depicted through solid lines due to intrinsic information loss. In fact, when performing regularization, we are discarding  $\mathbf{G}_R$  elements that are informative and contain valuable information for optimal ROI image reconstruction. However, for  $R = N$ , some performance enhancement can still be obtained, as shown for the A-OPT, U-IP-OPT, and A-IP-OPT curves in both Figs. 3-left and 3-center. These improvements are mainly attributed to the illumination optimization, as opposed

to the NO-OPT case (red curve and markers), which somehow allows us to obtain improvements in the image reconstruction procedure. Finally, Fig. 3-right depicts the results when the ROI is placed at a larger distance. In this case, provided that the number of channel's DOF decreases (i.e.,  $N_{\text{DOF}}^{(c)} \rightarrow N_{\text{DOF}}^{(i)}$ ), both regularization and optimization play a crucial role in improving the performance.

In fact, in this case, there is a trade-off between the joint effect of the thermal noise and image distortion leading to an optimal truncation index of  $R = 60$ . Considering this last scenario and fixing  $R = 60$ , Fig. 4 displays the estimated images, i.e., the  $\hat{\gamma}$  values, for the various optimization approaches. As anticipated, illumination design plays a pivotal role in enhancing performance for this configuration, and the proposed U-IP-OPT approach outperforms the others.

In Fig. 5, we assess the imaging performance using a different reference image, characterized by an increased irregularity and complexity, having  $N_{\text{DOF}}^{(i)} = 4$ . Specifically, we examine the cases where  $y_{\text{ROI}} = 15$  m and  $y_{\text{ROI}} = 23$  m, selecting  $R = 64$  and  $R = 58$  as the truncation indices corresponding to the minimum NMSE values. The illustration includes the worst-case scenario (NO REG-NO OPT) and the one yielding improved reconstruction for this particular image, i.e., U-IP-OPT. Remarkably, the scenario corresponding to  $y = 23$  m, which provided satisfactory reconstructions in Fig. 4, yields unsatisfactory results for this more complicated image having a higher  $N_{\text{DOF}}^{(i)}$ . This underscores the fundamental interdependence between  $N_{\text{DOF}}^{(c)}$  and  $N_{\text{DOF}}^{(i)}$ . In particular, to reconstruct highly complex images characterized by a high  $N_{\text{DOF}}^{(i)}$ , a channel with a correspondingly high rank, and thus a large  $N_{\text{DOF}}^{(c)}$  is essential, e.g.,  $N_{\text{DOF}}^{(c)} = 26$  as in Fig. 3-center.

### C. Imaging Performance Under Rician Fading Conditions

Given that, in realistic radio environments, additional scattered paths coexist with the direct LOS component, we have examined the monostatic setup under Rician fading conditions for the TX/RX-ROI link of interest. In this specific scenario, we

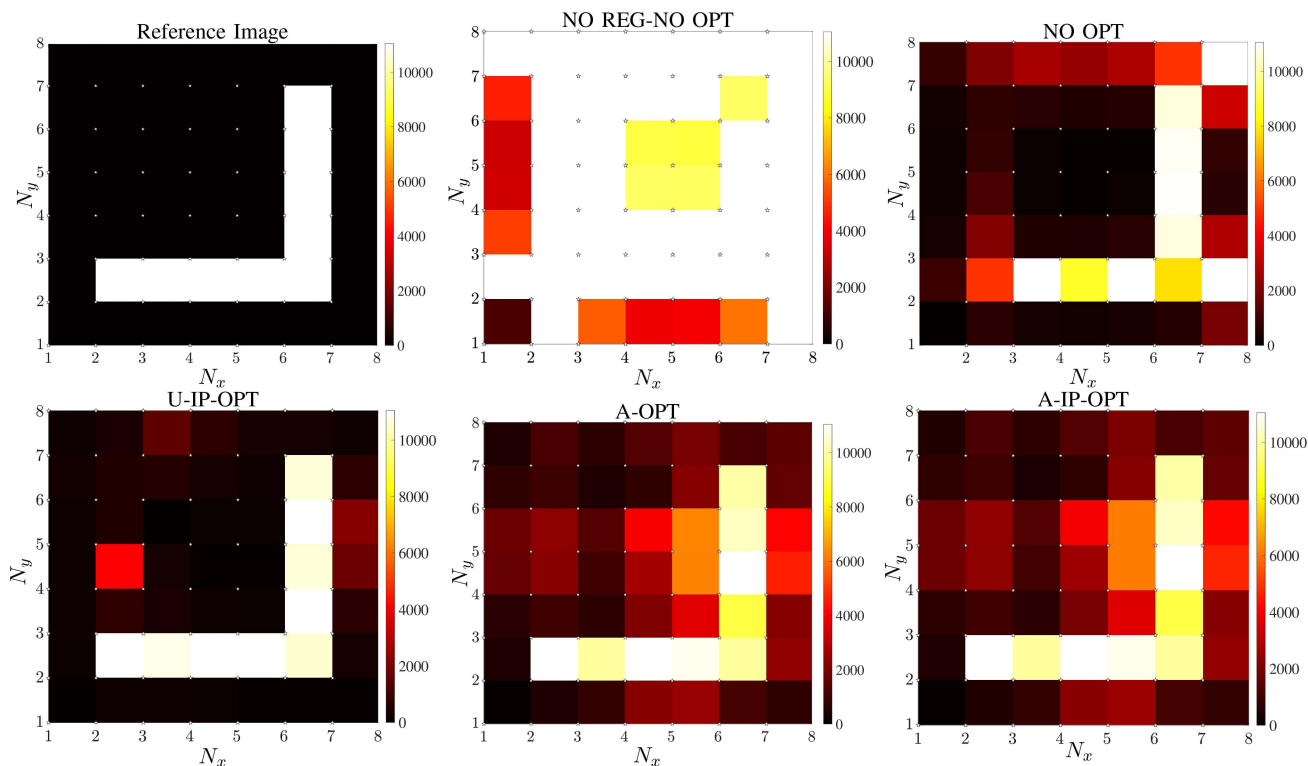


Fig. 4. Estimated images ( $\hat{\gamma}$ ) for  $R = 60$ ,  $y_{\text{ROI}} = 23$  m, different optimization approaches, and reference image with  $N_{\text{DOF}}^{(i)} = 2$ .

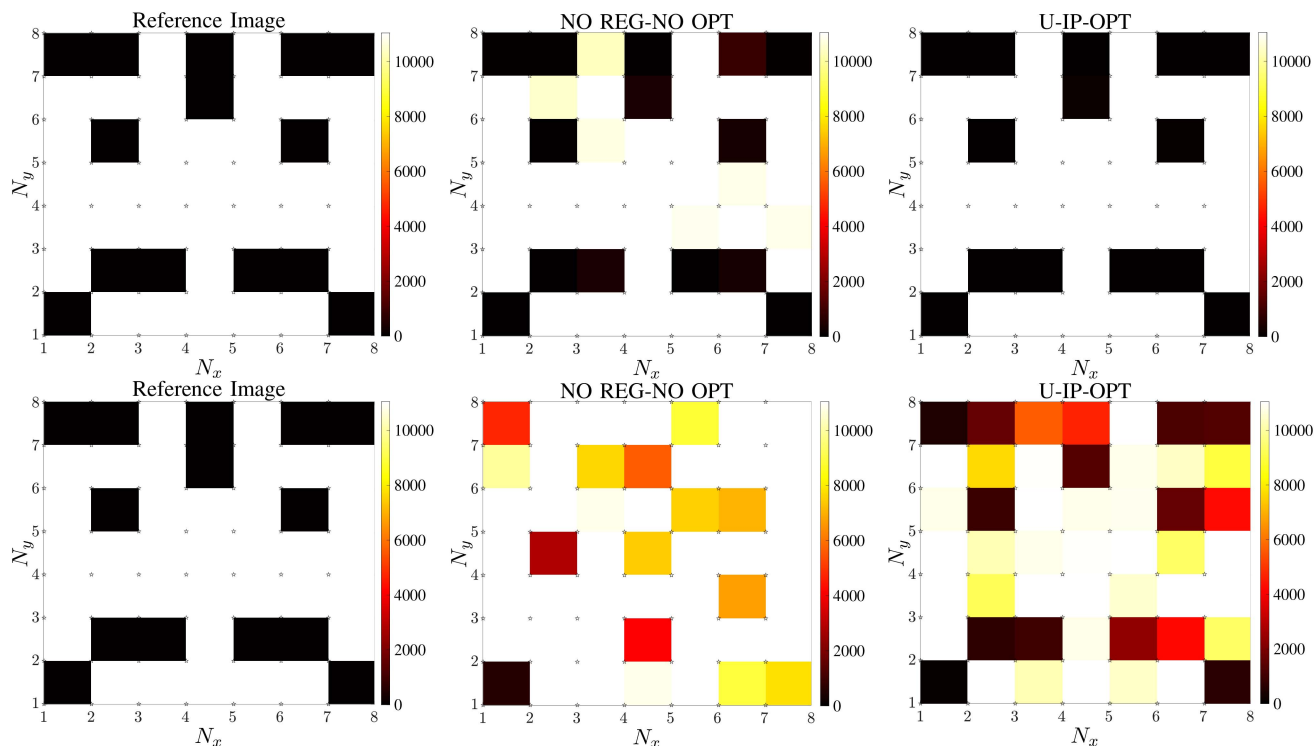


Fig. 5. Estimated images ( $\hat{\gamma}$ ) in the NO REG-NO OPT and IP-OPT cases for the selected reference image. The first row refers to the configuration  $y_{\text{ROI}} = 15$  m and  $R = 64$ , and the second one to the case  $y_{\text{ROI}} = 23$  m and  $R = 58$ . The reference image has  $N_{\text{DOF}}^{(i)} = 4$ .

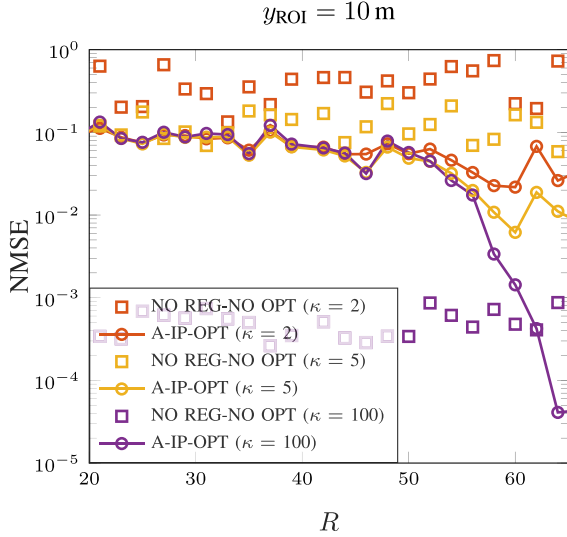


Fig. 6. NMSE as a function of the truncation index  $R$  selected for TSVD regularization for the monostatic setup and for different  $\kappa$  values, i.e.,  $\kappa = \{2, 5, 100\}$ . Two cases are shown, namely NO REG-NO OPT and A-IP-OPT.

have incorporated the effects of the Rician fading as follows

$$\mathbf{y} = \overline{\mathbf{G}}_{\mathbf{R}} \mathbf{\Gamma} \overline{\mathbf{G}}_{\mathbf{T}} \mathbf{x} + \mathbf{w}, \quad (51)$$

where

$$\overline{\mathbf{G}}_{\mathbf{T}} = \sqrt{\frac{\kappa_{\mathbf{T}}}{\kappa_{\mathbf{T}} + 1}} \mathbf{G}_{\mathbf{T}} + \sqrt{\frac{1}{\kappa_{\mathbf{T}} + 1}} \mathbf{S}_{\mathbf{T}}, \quad (52)$$

with  $\mathbf{S}_{\mathbf{T}} = \{s_{\mathbf{T},n,i}\} \in \mathbb{C}^{N \times N_{\mathbf{T}}}$  and  $s_{\mathbf{T},n,i} \sim \mathcal{CN}(0, |g_{\mathbf{T},n,i}|^2)$ . Similarly, it is

$$\overline{\mathbf{G}}_{\mathbf{R}} = \sqrt{\frac{\kappa_{\mathbf{R}}}{\kappa_{\mathbf{R}} + 1}} \mathbf{G}_{\mathbf{R}} + \sqrt{\frac{1}{\kappa_{\mathbf{R}} + 1}} \mathbf{S}_{\mathbf{R}}, \quad (53)$$

with  $\mathbf{S}_{\mathbf{R}} = \{s_{\mathbf{R},r,n}\} \in \mathbb{C}^{N_{\mathbf{R}} \times N}$  and  $s_{\mathbf{R},r,n} \sim \mathcal{CN}(0, |g_{\mathbf{R},r,n}|^2)$ . Given the monostatic setup, we set the Rician factor  $\kappa_{\mathbf{T}} = \kappa_{\mathbf{R}} = \kappa \geq 0$  to be identical for the TX/RX-ROI link and the reciprocal one. In Fig. 6, we reported the numerical results for the monostatic setup, having the same geometrical parameters as per Section VI-B and when the reference L-shaped image of Fig. 4 has to be reconstructed. The center of the TX/RX array is set in  $(0, 0, 0)$  m and the ROI center is located in  $(0, 10, 0)$  m. We assumed  $\kappa \in \{2, 5, 100\}$  and, for each of these values, we considered the NO REG-NO OPT and A-IP-OPT cases.

It is evident that, at lower values of  $\kappa$ , imaging performance is significantly influenced by strong fading. However, for  $\kappa = 100$ , improvements are more pronounced, despite not achieving the same level of NMSE as depicted in Fig. 3-left under LOS conditions. For instance, in the case of NO REG-NO OPT for  $\kappa = 100$ , the NMSE reaches approximately  $10^{-3}$ , whereas in Fig. 3-left, NMSE values around  $10^{-7}$  are attained. As intuitively predictable, fading strongly impacts the image reconstruction process, given that our approach is tailored for LOS conditions.

#### D. Imaging Performance for a Dataset of Randomly Generated Images

To further generalize our findings, and hence mitigate potential biases stemming from the specific reference image chosen, we have conducted additional simulations mirroring the configuration depicted in Fig. 3. This involved employing a monostatic LOS setup with three distinct link distances ( $y_{\text{ROI}} \in \{10, 15, 23\}$  m). In this additional analysis, we have generated a diverse dataset of images for reconstruction, all possessing the same DoF, that is,  $N_{\text{DOF}}^{(i)} = 4$ . Then, we run  $N_{\text{MC}}$  Monte Carlo experiments wherein each experiment considered a different image from the dataset alongside a new realization of AWGN. Consequently, at each iteration, the illumination signal optimization was repeated to accommodate the updated  $\gamma$  parameters corresponding to the current image. For comparison, we also examined the scenario where a unique reference image is utilized, mirroring the approach adopted in Fig. 3. However, in this instance, the selected reference image corresponds to the one illustrated in Fig. 5, maintaining an equivalent number of degrees of freedom ( $N_{\text{DOF}}^{(i)} = 4$ ) as the images within the dataset. The findings of this study are illustrated in Fig. 8, showcasing the standard deviation of the NMSE, i.e.,  $\sigma(\text{NMSE})$ , as a function of the truncation index  $R$  for both the image dataset case (dashed lines) and the single reference image case (continuous lines). The plot reveals a clear trend: as the distance between the TX/RX and the ROI expands, there is a corresponding increase in the standard deviation across all depicted scenarios. Specifically, the blue markers representing the case with no regularization and no optimization (NO REG-NO OPT) exhibit substantial variability, ranging from approximately  $10^{-8}$  for  $y = 10$  m in Fig. 8-left to around 10 for  $y = 23$  m in Fig. 8-right. This variability underscores the significant error fluctuations observed when transitioning from a strong near-field condition to the far-field regime in the absence of regularization or illumination optimization. Conversely, the scenarios in which illumination optimization at the TX/RX is employed demonstrate minimal variations as the link distance increases. This highlights the crucial role of selecting the optimal ROI illumination for ensuring high accuracy in the image reconstruction process and mitigating estimation errors. Remarkably, disregarding the case  $y = 10$  m, wherein the high channel rank renders both regularization and optimization futile, for the remaining two cases (Fig. 8-center and right), it is observable how the standard deviation for cases A-OPT and A-IP-OPT is markedly lower compared to the non-optimized cases, highlighting the usefulness of the proposed approaches. This is particularly evident for the  $y = 15$  m scenario, corresponding to a favorable propagation regime for our imaging purposes. Apart from this, for a fixed link distance, when comparing the dataset scenario with the utilization of a single image, it becomes evident that we achieve nearly identical performance concerning  $\sigma(\text{NMSE})$ , resulting in comparable “sometimes almost overlapping – accuracy levels in the estimation process. The primary disparity lies in the enhanced stability of the curves associated with the dataset employment, where the oscillations are slightly reduced compared to the single image case. However, this improvement comes at the

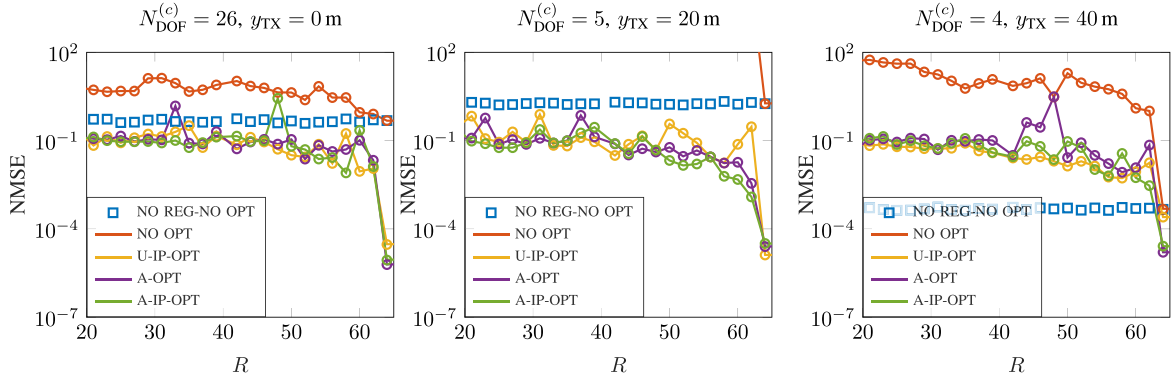


Fig. 7. NMSE as a function of the truncation index  $R$  selected when applying the TSVD to  $\mathbf{G}_R$  and different optimization techniques for the bistatic LOS setup. In this case, the receiver is located at  $(0, 0, -2)$  m, while the transmitting device is placed at  $(0, -y_{TX}, 2)$  m and three different distances from the ROI are tested, namely  $y_{TX} \in (0, 20, 40)$  m. Dotted ( $\circ$ ) and continuous ( $-$ ) lines correspond to the E-NMSE and T-NMSE, respectively, while the square markers denote the non-regularized case for benchmarking.  $N_{\text{DOF}}^{(c)}$  refers to the DoF of the illuminating channel  $\mathbf{G}_T$ .

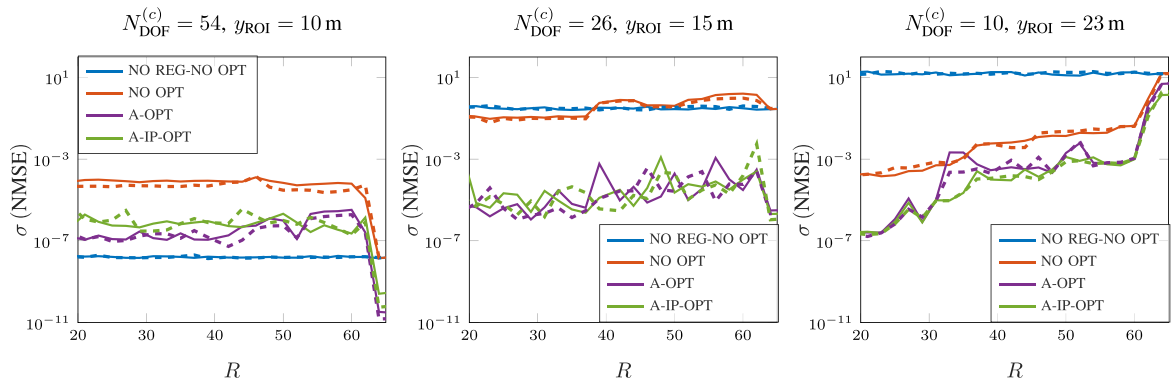


Fig. 8. Standard deviation of the NMSE as a function of the truncation index  $R$  selected when applying the TSVD to  $\mathbf{G}_R$  and different optimization techniques for the monostatic LOS setup. The TX/RX XL-MIMO array is located at  $(0, 0, 0)$  m and three distinct locations for the ROI are tested, namely  $y_{\text{ROI}} \in \{10, 15, 23\}$  m. The use of the random images dataset is indicated by dashed lines ( $- -$ ), while the use of a single reference image is denoted by solid lines ( $-$ ).

expense of significantly heightened computational time (almost threefold) and complexity. Consequently, a trade-off emerges between performance and execution time. Therefore, it is clear that the fundamental factor influencing the system's ability to reconstruct a given image more or less accurately is not so much associated with the number of ROI's images tested, but rather with the number of DoF of the image itself that we can calculate through PCA.

### E. Bistatic LOS Imaging Performance

We now assess the influence of the propagation regime on the effectiveness of the proposed optimization techniques for the illumination signal by considering a bistatic LOS configuration. To this purpose, we locate the TX array center in  $(0, y_{TX}, 2)$  m, with  $y_{TX} \in (0, 20, 40)$  m to test three distances from the ROI, which corresponds to  $N_{\text{DOF}}^{(c)} \in \{26, 5, 4\}$ , with  $N_{\text{DOF}}^{(c)}$  now referring to the TX-ROI link. The RX center was placed in  $(0, 0, -2)$  m, as per Fig. 1(b) and corresponding to  $N_{\text{DOF}}^{(c)} = 26$  for  $\mathbf{G}_R$ . In this setup, the ROI was kept in a fixed position centered in  $(0, 15, 0)$  m. In the following, we will refer

to the case where the transmitted image corresponds to the L-shaped picture as in Fig. 4.

Fig. 7 illustrates the E-NMSE and T-NMSE as a function of the truncation index  $R$  and the distance between the TX and the ROI. In these three cases, the best performance is obtained for the truncation index  $R = 64$ . As it can be noticed, when moving from a strong near-field to almost far-field regime (from left to right), the impact of the optimization of the illuminating signal becomes decreasingly important because of the reduced  $N_{\text{DOF}}^{(c)}$  of  $\mathbf{G}_T$  available for the optimization process. This result indicates that the most critical channel for imaging purposes is  $\mathbf{G}_R$ , whose DoF must be commensurate with the complexity of the image and, hence, it must be in the near-field. In contrast, imaging is still possible when the illuminating channel  $\mathbf{G}_T$  experiences the far-field. However, the benefits of optimizing the illuminating signal are appreciable only when  $\mathbf{G}_T$  is also in the near-field.

### F. RIS-Aided NLOS Imaging Performance

Finally, we analyze a monostatic NLOS scenario aided by a RIS. Specifically, we considered the system geometry of Fig. 2, where the XL-MIMO TX/RX is placed in  $(0, 0, 0)$  m, the RIS

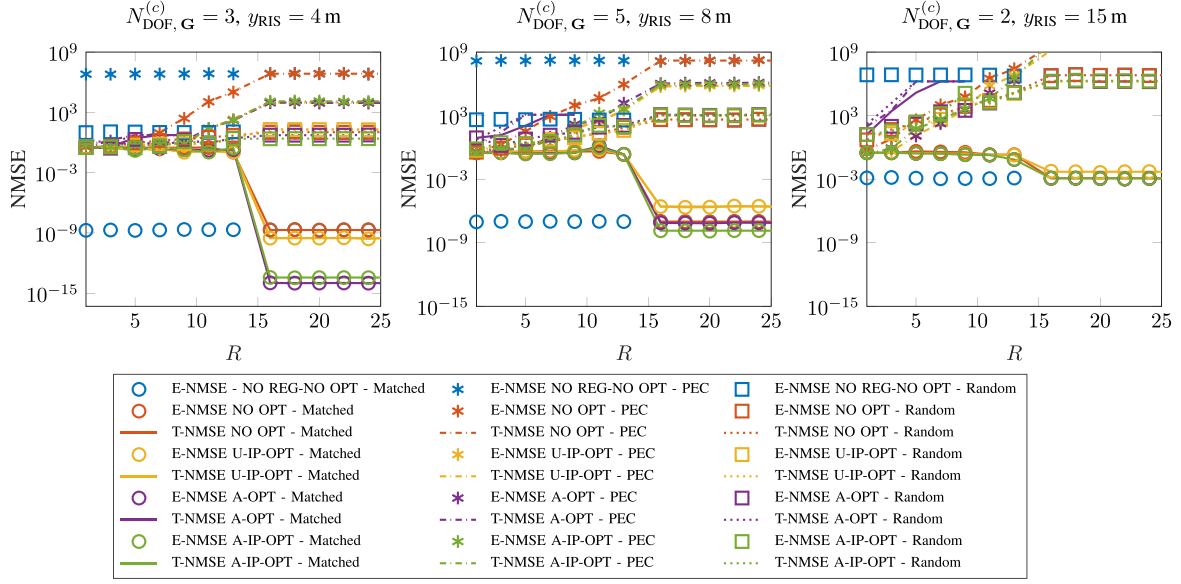


Fig. 9. NMSE as a function of the truncation index  $R$  selected when applying the TSVD to  $\mathbf{G}_R$  and different optimization techniques for the NLOS monostatic setup aided by a RIS. In this case, the TX/RX center is located at  $(0, 0, 0)$  m, while the RIS is placed at  $(0, y_{\text{RIS}}, 0)$  m with  $y_{\text{RIS}} \in (4, 8, 15)$  m. The legend delineates distinct RIS configurations in each column, arranged sequentially from left to right as matched, PEC, and random, respectively.

is located in  $(0, y_{\text{RIS}}, 0)$  m, with  $y_{\text{RIS}} \in (4, 8, 15)$  m, while the ROI's center is positioned in  $(0, 0, -9.5)$  m. These distances correspond to  $N_{\text{DOF}, \mathbf{G}_2}^{(c)} \in \{25, 5, 2\}$  for the TX-RIS link,  $N_{\text{DOF}, \mathbf{G}_1}^{(c)} \in \{3, 7, 13\}$  for the RIS-ROI link, hence resulting in  $N_{\text{DOF}, \mathbf{G}}^{(c)} \in \{3, 5, 2\}$  for the cascade channel, being  $N_{\text{DOF}, \mathbf{G}}^{(c)} = \min(N_{\text{DOF}, \mathbf{G}_1}^{(c)}, N_{\text{DOF}, \mathbf{G}_2}^{(c)})$ . In this setting, we considered a ROI having the same size and L-shape image as before but with  $N = 16$  scattering points, resulting in  $\Delta = 420\lambda$ . Moreover, three distinct RIS configurations are tested: (i) *matched*, which corresponds to the optimal configuration as per (48), (ii) *PEC*, i.e., the RIS acts like a perfect reflecting mirror, (iii) *random*, according to which independent random phase shifts are imposed at each RIS element. Analyzing Fig. 9, it becomes evident that the matched case yields superior performance compared to the other two RIS configurations, hence enabling the attainment of NMSE values several orders of magnitude smaller. This analysis underscores the fundamental importance of configuring the phase shift matrix  $\Phi$ , governing the behavior of the signal reflected by the RIS, to be perfectly adapted to wireless channels interconnecting the TX/RX to the ROI. In particular, as depicted in Fig. 9-left, the A-IP-OPT case, initialized with the analytical solution found in Section IV and featuring the RIS matched to both the incident (TX-RIS) and reflected (RIS-ROI) channels, facilitates the attainment of good imaging performance. Instead, no image reconstruction is possible when considering other RIS configurations (i.e., PEC or random).

Regarding the channels DoF,  $N_{\text{DOF}, \mathbf{G}_2}^{(c)}$  substantially decreases as the RIS approaches the far-field region, while  $N_{\text{DOF}, \mathbf{G}_1}^{(c)}$  progressively increases. This discrepancy arises because, in the former case, the TX-RIS link approaches the far-field limit, where  $N_{\text{DOF}, \mathbf{G}_2}^{(c)} = 1$ , whereas, in the latter case,

the RIS assumes a geometric configuration that enables more frontal, rather than oblique, illumination of the ROI. Consequently, it is evident that: (i) in Fig. 9-left, despite the small  $N_{\text{DOF}, \mathbf{G}}^{(c)}$  for the cascade channel, the joint impact of the optimal illumination performed by the TX and the RIS configuration tailored to the TX/RX-RIS and RIS-ROI channels leads to exceptionally low NMSE values; (ii) as the RIS moves away and approaches the far-field region, as shown in Fig. 9-(center, right), optimizing the RIS illumination at the TX no longer provides substantial benefits due to the small  $N_{\text{DOF}, \mathbf{G}_2}^{(c)}$ . Therefore, the RIS configuration plays a primary role in achieving low NMSE values, which, when matched, still allows for low errors in reconstructing the ROI scene. Given these considerations, the TX/RX-RIS channel  $\mathbf{G}_2$  emerges as the most critical component within the cascade channel  $\mathbf{G}$ , constituting the principal bottleneck for the NLOS imaging problem. In summary, in this NLOS scenario, the key factor for an effective imaging reconstruction lies in optimizing the  $\Phi$  matrix of the RIS to direct the reflected EM beam accurately toward the ROI.

## VII. CONCLUSION

We proposed a framework addressing the near-field imaging problem of a given ROI in a XL-MIMO communication scenario at millimeter-wave frequencies. Regularization techniques were applied to overcome ill-conditioning of the ISP. A min-max optimization approach was introduced to find a suitable illumination waveform minimizing an upper bound of the MSE on imaging estimation. Further, we derived the optimal RIS configuration for handling NLOS imaging scenarios. Numerical results demonstrated the feasibility of accurately estimating the ROI scattering coefficients, emphasizing the crucial interplay of

factors like the DoF of the channels, system geometry (monostatic and bistatic), illumination optimization, RIS configuration, and image complexity.

#### APPENDIX A MSE DERIVATION

Assuming that the only random vector is  $\mathbf{z}$  and by treating  $\gamma$  as an unknown deterministic vector, we can derive a closed-form expression of the MSE by starting from the covariance matrix definition in (20), i.e.,

$$\begin{aligned} \mathbf{C} &= \mathbb{E} \left\{ \left( \tilde{\mathbf{X}}^{-1} (\mathbf{H} - \mathbf{I}) \tilde{\mathbf{X}} \gamma \right) \left( \tilde{\mathbf{X}}^{-1} (\mathbf{H} - \mathbf{I}) \tilde{\mathbf{X}} \gamma \right)^H \right\} \\ &+ \mathbb{E} \left\{ \tilde{\mathbf{X}}^{-1} \mathbf{z} \left( \tilde{\mathbf{X}}^{-1} (\mathbf{H} - \mathbf{I}) \tilde{\mathbf{X}} \gamma \right)^H \right\} \\ &+ \mathbb{E} \left\{ \left( \tilde{\mathbf{X}}^{-1} (\mathbf{H} - \mathbf{I}) \tilde{\mathbf{X}} \gamma \right) \left( \tilde{\mathbf{X}}^{-1} \mathbf{z} \right)^H \right\} \\ &+ \mathbb{E} \left\{ \tilde{\mathbf{X}}^{-1} \mathbf{z} \left( \tilde{\mathbf{X}}^{-1} \mathbf{z} \right)^H \right\}, \end{aligned} \quad (54)$$

where we recall that  $\mathbf{z} = \tilde{\mathbf{G}}_R^\dagger \mathbf{w} = \mathbf{V} \tilde{\Sigma}^\dagger \mathbf{U}^H \mathbf{w}$ . By applying the expectation only to the random vectors and being  $\mathbb{E}\{\mathbf{z}\} = \mathbf{0}$ ,  $\mathbb{E}\{\mathbf{w} \mathbf{w}^H\} = \sigma^2 \mathbf{I}$  and  $\mathbf{U} \mathbf{U}^H = \mathbf{I}$ , we obtain

$$\begin{aligned} \mathbf{C} &= \left( \tilde{\mathbf{X}}^{-1} (\mathbf{H} - \mathbf{I}) \tilde{\mathbf{X}} \gamma \right) \left( \tilde{\mathbf{X}}^{-1} (\mathbf{H} - \mathbf{I}) \tilde{\mathbf{X}} \gamma \right)^H \\ &+ \sigma^2 \tilde{\mathbf{X}}^{-1} \mathbf{V} \tilde{\Sigma}^\dagger \left( \tilde{\Sigma}^\dagger \right)^H \mathbf{V}^H \left( \tilde{\mathbf{X}}^{-1} \right)^H. \end{aligned} \quad (55)$$

Let

$$\begin{aligned} \mathbf{q} &= \tilde{\mathbf{X}}^{-1} (\mathbf{H} - \mathbf{I}) \tilde{\mathbf{X}} \gamma \\ &= \begin{bmatrix} (h_{11} - 1)\gamma_1 + \sum_{i \neq 1} \tilde{x}_1^{-1} h_{1i} \tilde{x}_i \gamma_i \\ (h_{22} - 1)\gamma_2 + \sum_{i \neq 2} \tilde{x}_2^{-1} h_{2i} \tilde{x}_i \gamma_i \\ \vdots \\ (h_{NN} - 1)\gamma_N + \sum_{i \neq N} \tilde{x}_N^{-1} h_{N,i} \tilde{x}_i \gamma_i \end{bmatrix}. \end{aligned} \quad (56)$$

Then

$$\text{tr}(\mathbf{q} \mathbf{q}^H) = \sum_{n=1}^N \left| (h_{n,n} - 1)\gamma_n + \sum_{\substack{i=1 \\ i \neq n}}^N \tilde{x}_n^{-1} h_{n,i} \tilde{x}_i \gamma_i \right|^2, \quad (58)$$

where

$$h_{n,i} = [\mathbf{H}]_{ni} = [\mathbf{V} \mathbf{\Lambda} \mathbf{V}^H]_{ni} = \left[ \sum_{k=1}^K \omega_k^{-1} \mathbf{v}_k \mathbf{v}_k^H \right]_{ni}, \quad (59)$$

with  $\omega_k^{-1}$  being the elements along the diagonal of  $\mathbf{\Lambda}$  as per (17), i.e., its eigenvalues, and  $\mathbf{v}_k = [v_{1k}, v_{2k}, \dots, v_{Nk}]^T$  being the  $k$ -th eigenvector of  $\mathbf{V}$ .

Let us now consider the second term in (55) related to the receiver noise. We can express it as

$$\begin{aligned} \mathbf{N} &= \sigma^2 \tilde{\mathbf{X}}^{-1} \mathbf{V} \tilde{\Sigma}^\dagger \left( \tilde{\Sigma}^\dagger \right)^H \mathbf{V}^H \left( \tilde{\mathbf{X}}^{-1} \right)^H \\ &= \sigma^2 \tilde{\mathbf{X}}^{-1} \left( \sum_{k=1}^K \frac{1}{(\omega_k \xi_k)^2} \cdot \mathbf{v}_k \mathbf{v}_k^H \right) \left( \tilde{\mathbf{X}}^{-1} \right)^H, \end{aligned} \quad (60)$$

and its trace is given by

$$\begin{aligned} \text{tr}(\mathbf{N}) &= \sum_{n=1}^N \frac{\sigma^2}{|\tilde{x}_n|^2} \left[ \sum_{k=1}^K \frac{1}{(\omega_k \xi_k)^2} \mathbf{v}_k \mathbf{v}_k^H \right]_{n,n} \\ &= \sum_{n=1}^N \frac{\sigma^2}{|\tilde{x}_n|^2} \sum_{k=1}^K \frac{1}{(\omega_k \xi_k)^2} |v_{n,k}|^2. \end{aligned} \quad (61)$$

Finally,

$$\text{MSE}(\mathbf{x}) = \text{tr}(\mathbf{C}) = \text{tr}(\mathbf{q} \mathbf{q}^H) + \text{tr}(\mathbf{N}), \quad (62)$$

resulting in (21).

#### APPENDIX B

##### OPTIMIZATION OF THE ILLUMINATION TRANSMIT SIGNAL

In this appendix, we solve the minimization problem in (27). To this end, we can write  $g(\mathbf{x}) = \sum_{n=1}^N \frac{\alpha_n}{b_n}$ , where  $b_n = |\tilde{x}_n|^2$  and  $\alpha_n \triangleq \sigma^2 \sum_{k=1}^K (\omega_k \xi_k)^{-2} |v_{n,k}|^2$ . Moreover, let us write  $\tilde{x}_n$  as  $\tilde{x}_n = \mathbf{g}_{T,n} \mathbf{x}$ , where  $\mathbf{g}_{T,n}$  denotes the  $n$ -th row of  $\mathbf{G}_T$ . Consequently, the sum  $\sum_n b_n$  becomes

$$\sum_n b_n = \sum_n \mathbf{g}_{T,n} \mathbf{x} \mathbf{x}^H \mathbf{g}_{T,n}^H. \quad (63)$$

Hence, the optimization problem becomes

$$b_n^* = \arg \min_{b_n} g(b_n) \quad (64)$$

$$\text{s.t.} \quad \sum_n b_n \leq P, \quad (65)$$

where  $P$  represents the upper bound of the term  $\sum_n |\tilde{x}_n|^2$  given by  $P = P_T \cdot \sum_n \mathbf{g}_{T,n} \mathbf{g}_{T,n}^H$ .

By considering the Karush-Kuhn-Tucker (KKT) conditions, the solution is given by

$$b_n = \frac{P \sqrt{\alpha_n}}{\sum_n \sqrt{\alpha_n}}, \quad (66)$$

and it corresponds to the following MSE expression associated to the noise presence only

$$\text{MSE}_{(noise)}^{\text{opt}} = \frac{1}{P} \left| \sum_n \sqrt{\alpha_n} \right|^2. \quad (67)$$

#### REFERENCES

- [1] H. Sariahdeen, N. Saeed, T. Y. Al-Naffouri, and M.-S. Alouini, "Next generation terahertz communications: A rendezvous of sensing, imaging, and localization," *IEEE Commun. Mag.*, vol. 58, no. 5, pp. 69–75, May 2020.
- [2] F. Liu et al., "Seventy years of radar and communications: The road from separation to integration," *IEEE Signal Process. Mag.*, vol. 40, no. 5, pp. 106–121, Jul. 2023.
- [3] M. Boyarsky et al., "Electronically steered metasurface antenna," *Sci. Rep.*, vol. 11, no. 1, Feb. 2021, Art. no. 4693.
- [4] M. Faenzi et al., "Metasurface antennas: New models, applications and realizations," *Sci. Rep.*, vol. 9, no. 1, Jul. 2019, Art. no. 10178.
- [5] Z. Wang et al., "Extremely large-scale MIMO: Fundamentals, challenges, solutions, and future directions," *IEEE Wireless Commun.*, vol. 31, no. 3, pp. 117–124, Jun. 2024.
- [6] H. Lu et al., "A tutorial on near-field XL-MIMO communications towards 6G," *IEEE Commun. Surv. Tutor.*, Apr. 2024.

- [7] F. Guidi and D. Dardari, "Radio positioning with EM processing of the spherical wavefront," *IEEE Trans. Wireless Commun.*, vol. 20, no. 6, pp. 3571–3586, Jun. 2021.
- [8] H. Zhang, N. Shlezinger, F. Guidi, D. Dardari, and Y. C. Eldar, "6G wireless communications: From far-field beam steering to near-field beam focusing," *IEEE Commun. Mag.*, vol. 61, no. 4, pp. 72–77, Apr. 2023.
- [9] E. Björnson et al., "Massive MIMO is a reality What is next?: Five promising research directions for antenna arrays," *Digit. Signal Process.*, vol. 94, pp. 3–20, Jun. 2019.
- [10] D. Dardari, "Communicating with large intelligent surfaces: Fundamental limits and models," *IEEE J. Sel. Areas Commun.*, vol. 38, no. 11, pp. 2526–2537, Nov. 2020.
- [11] H. Zhang, N. Shlezinger, F. Guidi, D. Dardari, M. F. Imani, and Y. C. Eldar, "Beam focusing for near-field multiuser MIMO communications," *IEEE Trans. Wireless Commun.*, vol. 21, no. 9, pp. 7476–7490, Sep. 2022.
- [12] J. An, C. Yuen, C. Huang, M. Debbah, H. V. Poor, and L. Hanzo, "A tutorial on holographic MIMO communications—part I: Channel modeling and channel estimation," *IEEE Commun. Lett.*, vol. 27, no. 7, pp. 1664–1668, Jul. 2023.
- [13] D. Dardari and N. Decarli, "Holographic communication using intelligent surfaces," *IEEE Commun. Mag.*, vol. 59, no. 6, pp. 35–41, Jun. 2021.
- [14] S. Palmucci, A. Guerra, A. Abrardo, and D. Dardari, "Two-timescale joint precoding design and RIS optimization for user tracking in near-field MIMO systems," *IEEE Trans. Signal Process.*, vol. 71, pp. 3067–3082, 2023.
- [15] A. Elzanaty, A. Guerra, F. Guidi, and M. -S. Alouini, "Reconfigurable intelligent surfaces for localization: Position and orientation error bounds," *IEEE Trans. Signal Process.*, vol. 69, pp. 5386–5402, 2021.
- [16] A. Guerra, F. Guidi, D. Dardari, and P. M. Djurić, "Near-field tracking with large antenna arrays: Fundamental limits and practical algorithms," *IEEE Trans. Signal Process.*, vol. 69, pp. 5723–5738, 2021.
- [17] J. He, A. Fakhreddine, C. Vanwysberghe, H. Wymeersch, and G. C. Alexandropoulos, "3D localization with a single partially-connected receiving RIS: Positioning error analysis and algorithmic design," *IEEE Trans. Veh. Technol.*, vol. 72, no. 10, pp. 13190–13202, Oct. 2023.
- [18] F. Liu et al., "Integrated sensing and communications: Toward dual-functional wireless networks for 6G and beyond," *IEEE J. Sel. Areas Commun.*, vol. 40, no. 6, pp. 1728–1767, Jun. 2022.
- [19] N. González-Prelcic et al., "The integrated sensing and communication revolution for 6G: Vision, techniques, and applications," *Proc. IEEE*, early access, May 22, 2024, doi: [10.1109/JPROC.2024.3397609](https://doi.org/10.1109/JPROC.2024.3397609).
- [20] F. Guidi, A. Guerra, and D. Dardari, "Personal mobile radars with millimeter-wave massive arrays for indoor mapping," *IEEE Trans. Mobile Comput.*, vol. 15, no. 6, pp. 1471–1484, Jun. 2016.
- [21] C. Huang, A. Zappone, G. C. Alexandropoulos, M. Debbah, and C. Yuen, "Reconfigurable intelligent surfaces for energy efficiency in wireless communication," *IEEE Trans. Wireless Commun.*, vol. 18, no. 8, pp. 4157–4170, Aug. 2019.
- [22] M. D. Renzo et al., "Smart radio environments empowered by reconfigurable AI meta-surfaces: An idea whose time has come," *EURASIP J. Wireless Commun. Netw.*, vol. 2019, no. 1, pp. 1–20, May 2019.
- [23] T. Gong et al., "Holographic MIMO communications: Theoretical foundations, enabling technologies, and future directions," *IEEE Commun. Surv. Tut.*, vol. 26, no. 1, pp. 196–257, Firstquarter 2024.
- [24] X. Chen, *Computational Methods for Electromagnetic Inverse Scattering*. Hoboken, NJ, USA: Wiley, 2018.
- [25] M. Bertero, P. Boccacci, and C. D. Mol, *Introduction to Inverse Problems in Imaging*. Boca Raton, FL, USA: CRC Press, 2021.
- [26] L. Crocco, I. Catapano, L. D. Donato, and T. Isernia, "The linear sampling method as a way to quantitative inverse scattering," *IEEE Trans. Antennas Propag.*, vol. 60, no. 4, pp. 1844–1853, Apr. 2012.
- [27] J. M. Lopez-Sanchez and J. Fortuny-Guasch, "3-D radar imaging using range migration techniques," *IEEE Trans. Antennas Propag.*, vol. 48, no. 5, pp. 728–737, May 2000.
- [28] C. Cafforio, C. Prati, and F. Rocca, "SAR data focusing using seismic migration techniques," *IEEE Trans. Aerosp. Electron. Syst.*, vol. 27, no. 2, pp. 194–207, Mar. 1991.
- [29] S. k. Doddalla and G. C. Trichopoulos, "Non-line of sight terahertz imaging from a single viewpoint," in *Proc. IEEE/MTT Int. Microw. Symp.*, 2018, pp. 1527–1529.
- [30] A. Broquetas, J. Palau, L. Jofre, and A. Cardama, "Spherical wave near-field imaging and radar cross-section measurement," *IEEE Trans. Antennas Propag.*, vol. 46, no. 5, pp. 730–735, May 1998.
- [31] Z. Sun, C. Li, S. Gu, and G. Fang, "Fast three-dimensional image reconstruction of targets under the illumination of Terahertz Gaussian beams with enhanced phase-shift migration to improve computation efficiency," *IEEE Trans. Terahertz Sci. Technol.*, vol. 4, no. 4, pp. 479–489, Aug. 2014.
- [32] M. Zhou, Y. Alfdahl, and X. Chen, "Optimal spatial sampling criterion in a 2D THz holographic imaging system," *IEEE Access*, vol. 6, pp. 8173–8177, 2018.
- [33] J. Gao, Y. Qin, B. Deng, H. Wang, and X. Li, "Novel efficient 3D short-range imaging algorithms for a scanning 1D-MIMO array," *IEEE Trans. Image Process.*, vol. 27, no. 7, pp. 3631–3643, Jul. 2018.
- [34] X. Zhuge and A. G. Yarovoy, "Three-dimensional near-field MIMO array imaging using range migration techniques," *IEEE Trans. Image Process.*, vol. 21, no. 6, pp. 3026–3033, Jun. 2012.
- [35] C. Ma, T. S. Yeo, C. S. Tan, and Z. Liu, "Three-dimensional imaging of targets using colocated MIMO radar," *IEEE Trans. Geosci. Remote Sens.*, vol. 49, no. 8, pp. 3009–3021, Aug. 2011.
- [36] J. N. Mait, G. W. Euliss, and R. A. Athale, "Computational imaging," *Adv. Opt. Photon.*, vol. 10, no. 2, pp. 409–483, 2018.
- [37] K. Khare, M. Butola, and S. Rajora, *Fourier Optics and Computational Imaging*. Berlin, Germany: Springer, 2015.
- [38] O. Cossairt, M. Gupta, and S. K. Nayar, "When does computational imaging improve performance?," *IEEE Trans. Image Process.*, vol. 22, no. 2, pp. 447–458, Feb. 2013.
- [39] T. D. Mast, A. I. Nachman, and R. C. Waag, "Focusing and imaging using eigenfunctions of the scattering operator," *J. Acoust. Soc. Amer.*, vol. 102, no. 2, pp. 715–725, Feb. 1997.
- [40] Y. Cui and G. C. Trichopoulos, "Seeing around obstacles using active terahertz imaging," *IEEE Trans. Terahertz Sci. Technol.*, May 2024.
- [41] J. L. Walker, "Range-Doppler imaging of rotating objects," *IEEE Trans. Aerosp. Electron. Syst.*, vol. 16, no. 1, pp. 23–52, Jan. 1980.
- [42] A. F. Yegulalp, "Fast backprojection algorithm for synthetic aperture radar," in *Proc. IEEE Radar Conf.*, 1999, pp. 60–65.
- [43] Y. Na, Y. Lu, and H. Sun, "A comparison of back-projection and range migration algorithms for ultra-wideband SAR imaging," in *Proc. 4th IEEE Workshop Sensor Array Multichannel Process.*, 2006, pp. 320–324.
- [44] C. Prati, A. M. Guarnieri, and F. Rocca, "Spot mode SAR focusing with the omega-K technique," in *Proc. 11th Annu. Int. Geosci. Remote Sens. Symp.*, 1991, pp. 631–634.
- [45] R. K. Raney, H. Runge, R. Bamler, I. G. Cumming, and F. H. Wong, "Precision SAR processing using chirp scaling," *IEEE Trans. Geosci. Remote Sens.*, vol. 32, no. 4, pp. 786–799, Jul. 1994.
- [46] J. Fortuny, A. J. Sieber, J. Palau, and A. Broquetas, "QUICKSAR: A near field linear/inverse synthetic aperture radar processor," in *Proc. Prog. Electromagn. Res. Symp.*, Noordwijk, The Netherlands, 1994.
- [47] J. Wang, K. Liu, Y. Cheng, and H. Wang, "Three-dimensional target imaging based on vortex stripmap SAR," *IEEE Sens. J.*, vol. 19, no. 4, pp. 1338–1345, Feb. 2019.
- [48] M. I. Duersch and D. G. Long, "Analysis of time-domain back-projection for stripmap SAR," *Int. J. Remote Sens.*, vol. 36, no. 8, pp. 2010–2036, Apr. 2015.
- [49] R. H. Stolt, "Migration by fourier transform," *Geophysics*, vol. 43, no. 1, pp. 23–48, Feb. 1978.
- [50] S. S. A. Ahmed, *Electronic Microwave Imaging With Planar Multistatic Arrays*. Berlin, Germany: Logos Verlag, 2014.
- [51] I. Manisali, O. Oral, and F. S. Oktm, "Efficient physics-based learned reconstruction methods for real-time 3D near-field MIMO radar imaging," *Digit. Signal Process.*, vol. 144, 2023, Art. no. 104274.
- [52] Q. Cheng, A. A. Ihalage, Y. Liu, and Y. Hao, "Compressive sensing radar imaging with convolutional neural networks," *IEEE Access*, vol. 8, pp. 212917–212926, 2020.
- [53] M. Wang et al., "RMIST-Net: Joint range migration and sparse reconstruction network for 3-D mmW imaging," *IEEE Trans. Geosci. Remote Sens.*, vol. 60, 2022, Art. no. 5205117.
- [54] A. Kirmani, T. Hutchison, J. Davis, and R. Raskar, "Looking around the corner using transient imaging," in *Proc. IEEE 12th Int. Conf. Comput. Vis.*, 2009, pp. 159–166.
- [55] W. Gong et al., "Three-dimensional ghost imaging Lidar via sparsity constraint," *Sci. Rep.*, vol. 6, no. 1, May 2016, Art. no. 26133.
- [56] B. Mamandipoor, U. Madhow, and A. Arbabian, "2D mm-wave imaging based on singular value decomposition," in *Proc. IEEE MTT-S Int. Microw. Symp.*, 2019, pp. 536–539.
- [57] R. Pierri and F. Soldovieri, "On the information content of the radiated fields in the near zone over bounded domains," *Inverse Prob.*, vol. 14, no. 2, Jan. 1998, Art. no. 321.

- [58] O. Bucci, L. Crocco, and T. Isernia, "Improving the reconstruction capabilities in inverse scattering problems by exploitation of close-proximity setups," *JOSA A*, vol. 16, no. 7, pp. 1788–1798, Jul. 1999.
- [59] H. Luo and A. Alkhateeb, "Integrated imaging and communication with reconfigurable intelligent surfaces," in *Proc. 57th Asilomar Conf. Signals, Syst., Comput.*, Oct. 2023, pp. 151–156.
- [60] Y. He, D. Zhang, and Y. Chen, "High-resolution WiFi imaging with reconfigurable intelligent surfaces," *IEEE Internet Things J.*, vol. 10, no. 2, pp. 1775–1786, Jan. 2023.
- [61] M. O'Toole, D. B. Lindell, and G. Wetzstein, "Confocal non-line-of-sight imaging based on the light-cone transform," *Nature*, vol. 555, no. 7696, pp. 338–341, Mar. 2018.
- [62] Y. Tao and Z. Zhang, "Distributed computational imaging with reconfigurable intelligent surface," in *Proc. IEEE Int. Conf. Wireless Commun. Signal Process.*, 2020, pp. 448–454.
- [63] Y. Jiang, F. Gao, Y. Liu, S. Jin, and T. Cui, "Near field computational imaging with RIS generated virtual masks," *IEEE Trans. Antennas Propag.*, Apr. 2024.
- [64] X. Zhang, H. Zhang, and Y. C. Eldar, "Near-field sparse channel representation and estimation in 6G wireless communications," *IEEE Trans. Commun.*, vol. 72, no. 1, pp. 450–464, Jan. 2024.
- [65] Y. Lu and L. Dai, "Near-field channel estimation in mixed LoS/NLoS environments for extremely large-scale MIMO systems," *IEEE Trans. Commun.*, vol. 71, no. 6, pp. 3694–3707, Jun. 2023.
- [66] Z. Hu, C. Chen, Y. Jin, L. Zhou, and Q. Wei, "Hybrid-field channel estimation for extremely large-scale massive MIMO system," *IEEE Commun. Lett.*, vol. 27, no. 1, pp. 303–307, Jan. 2023.
- [67] M. Biguesh and A. B. Gershman, "Training-based MIMO channel estimation: A study of estimator tradeoffs and optimal training signals," *IEEE Trans. Signal Process.*, vol. 54, no. 3, pp. 884–893, Mar. 2006.
- [68] E. Björnson, Ö. T. Demir, and L. Sanguinetti, "A primer on near-field beamforming for arrays and reconfigurable intelligent surfaces," in *Proc. 55th Asilomar Conf. Signals Syst. Comput.*, 2021, pp. 105–112.
- [69] S. Lipschutz and M. L. Lipson, *Linear Algebra 4th Ed.* New York, NY, USA: McGraw-Hill, 2001.
- [70] G. H. Golub and C. F. V. Loan, "Matrix computations (3rd edition)," The John Hopkins University, Baltimore, 1996.
- [71] O. M. Bucci and G. Franceschetti, "On the degrees of freedom of scattered fields," *IEEE Trans. Antennas Propag.*, vol. 37, no. 7, pp. 918–926, Jul. 1989.
- [72] A. Och et al., "High-resolution millimeter-wave tomography system for nondestructive testing of low-permittivity materials," *IEEE Trans. Microw. Theory Techn.*, vol. 69, no. 1, pp. 1105–1113, Jan. 2021.
- [73] B.-Y. Wang and B.-Y. Xi, "Some inequalities for singular values of matrix products," *Linear Algebra Appl.*, vol. 264, pp. 109–115, Oct. 1997.
- [74] G. Bartoli et al., "Spatial multiplexing in near field MIMO channels with reconfigurable intelligent surfaces," *IET Signal Process.*, vol. 17, no. 3, Mar. 2023, Art. no. e12195.
- [75] R. H. Byrd, M. E. Hribar, and J. Nocedal, "An interior point algorithm for large-scale nonlinear programming," *SIAM J. Optim.*, vol. 9, no. 4, pp. 877–900, Sep. 1999.
- [76] O. Solomon et al., "Deep unfolded robust PCA with application to clutter suppression in ultrasound," *IEEE Trans. Med. Imag.*, vol. 39, no. 4, pp. 1051–1063, Apr. 2020.